ANALYSIS AND TESTING OF THE TRANSVERSE TENDON BEHAVIOR IN THE VARINA-ENON

Mehrshid Mohammadian

Thesis submitted to the faculty of the Virginia Polytechnic Institute and State University
in partial fulfillment of the requirements for the degree of

Master of Science
In
Civil Engineering

Carin L. Roberts-Wollmann, Chair
Ioannis Koutromanos
Matthew H. Hebdon

February 18, 2019
Blacksburg, Virginia

ANALYSIS AND TESTING OF THE TRANSVERSE TENDON BEHAVIOR IN THE VARINA-ENON

Mehrshid Mohammadian

ABSTRACT

Post-tensioned segmental concrete bridges have been used in the United States since the mid 80's. Post tensioning is very economical and efficient for bridges with very long spans. A segmental concrete bridge uses post-tensioning to connect concrete bridge segments and make a long span bridge. A problem that has occurred in some segmental concrete bridges is the corrosion of the post-tensioned strands. A tendon failure can be detrimental to service level bridge performance and reduce the flexural strength.

The Varina-Enon Bridge has a history of corrosion related issues and the objective of this project was to investigate the consequences of transverse tendons rupture. In addition, to determine the behavior of tendons with grouted duct and smoot duct when a stand broke. Also, the results of this project identifies if the bridge can perform adequately with no repair or if these failures would develop problems in the long term.

A full scale specimen of a post-tensioned slab with two tendons was built at the laboratory. The full scale specimen was built to contain tendons similar to top flange near the delta frames in the Varina-Enon Bridge, where a transverse tendon was broken. An artificial corrosion process was conducted to corrode the tendons and investigate the effect of break on the slab. The specimen was instrumented with BDI strain gauges to monitor the behavior of the specimen, when the strand rupture occurred due to the accelerated corrosion. In addition, a finite element model was designed similar to the full scale specimen to compare the collected data with the data obtained from the analysis.

ANALYSIS AND TESTING OF THE TRANSVERSE TENDON BEHAVIOR IN THE VARINA-ENON

Mehrshid Mohammadian

GENERAL AUDIENCE ABSTRACT

Bridges play a very important role in the Transportation Systems all over the world. According to American Society of Civil Engineering (ASCE), United States bridges get a C+ grade. The ASCE rating indicates that the US bridges need to be built more efficiently and be monitored more frequently. Regular inspection of bridges is very essential and will be beneficial in many ways. For instance, engineers can detect the possible flaws and problems that are in the bridge such as corrosion in structural elements. It is important to address these issues since these bridges are in service and being used by the public. Based on how serious the issues are, engineers will decide if the bridge can perform adequately with repair or it is is structurally inefficient and needs to be replaced. Moreover, rehabilitations method to keep the structure in service will save a lot of money compare to replacing the bridge.

The Varian Enon Bridge, which carries Interstate 295 across the James River in Richmond, is a critical link in Richmond transportation a In the recent inspections of this bridge, Virginia Department of Transportations (VDOT) detected abnormal behavior of few structural elements. In this research, a full scale mock-up of a section of the Varina Enon Bridge was built at the lab. The purpose of this project was to conduct testing on the mock-up to investigate the cause of abnormal behavior of these few structural elements similar to the ones in Varina Enon Bridge. Furthermore, a final report was prepared for VDOT to decide if the bridge will perform adequately with no strengthening or providing forewarning of trouble that could develop with time.

ACKNOWLEDGEMENT

I would like to express my sincere gratitude to my advisors Dr. Carin L. Roberts-Wollmann and Dr. Ioannis Koutromanos for their continuous support. I've learned a lot from my both advisors, and I could not have imagined having a better advisors and mentors. I appreciate all the guidance from Dr. Wollmann and how it would make me a better engineer in the future.

In addition, I would like to thank my parents Hamidreza Mohammadian and Mitra Mohammadian for their continuous support throughout my education.

TABLE OF CONTENTS

LIST OF FIGURES

LIST OF TABLES

1. INTRODUCTION

1.1 General

Post-tensioned segmental concrete bridges have been used in the United States since the mid 80's. Post tensioning is very economical and efficient for bridges with very long spans such as 60 ft – 240 ft. A segmental concrete bridge uses post-tensioning to connect concrete bridge segments and make a long span bridge. Trapezoidal box girder with cantilever winged are the most popular cross sections for segmental concrete bridges. The most common problem with the segmental concrete bridges is the corrosion of the post-tensioned strands. A tendon failure can be detrimental to the service level performance and reduce the flexural strength. Evidence shows the failure occurs when there are grouting deficiencies in the duct. The purpose of this project is to investigate the consequences of tendon failure in the Varina-Enon Bridge.

1.2 Background

The Varina-Enon Bridge was built in 1990 and carries Interstate 295 across the James River south of Richmond, VA and Figure 1-1 shows a view of the Varina-Enon Bridge. The bridge is 4,680 ft long and comprises two separate approach bridges; north- and south-bound. The Varina-Enon Bridge is a post-tensioned segmental concrete bridge with two different cross sections for approach and main spans. The approach structure includes six 150 ft long span that are erected using span-by-span segmental construction. Each span includes seven segments that are tied together by eight external post-tensioning tendons. Figure 1-2 shows the cross-section of the approach spans. This bridge

has a 630 ft long cable-stayed main span, which consists of two trapezoidal box girders that are tied together with discrete delta frames at the cable anchoring locations. The Varina Enon was the first bridge in the world to use precast concrete delta frames and is the second cable-stayed bridge in the United States.

Figure 1-1 The Varina-Enon Bridge (Figg, 2019)

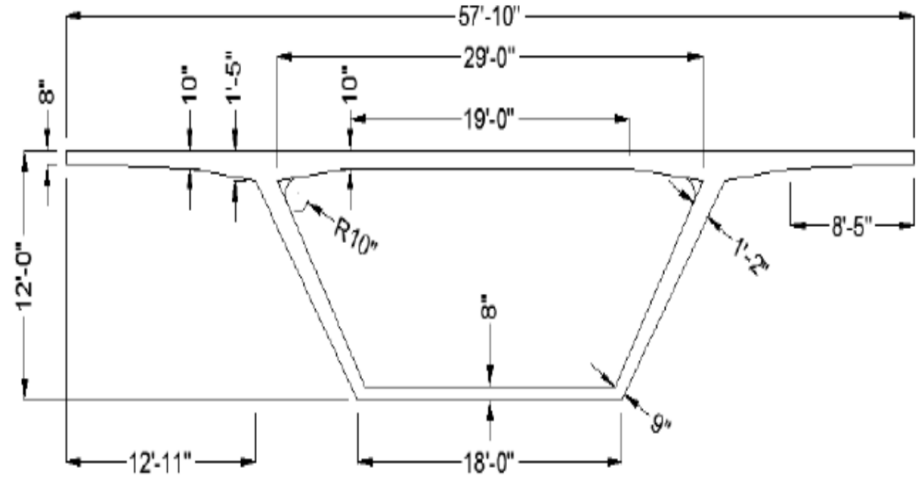

Figure 1-2 Cross Section dimensions of the approach spans of the Varina-Enon Bridge (Maguire M, 2013)

The main cable stayed span contains transverse tendons that are both used to support the long cantilever wings of the two independent boxes, and to tie the boxes to the delta frames which anchor the single plane of stays. These transverse tendons are important because they ensure that concrete stresses in the tension members of each transverse frame are in compression. The transverse frame comprises the delta frame, the webs and top and bottom slab of the boxes, and diagonal struts within the boxes. Figure 1-3 shows transverse frame with the members shown in tension and in compression when the bridge is subjected to the dead loads. Therefore, the transverse tendons play a critical role in the main cable stayed span and it is very important to maintain them in a good condition.

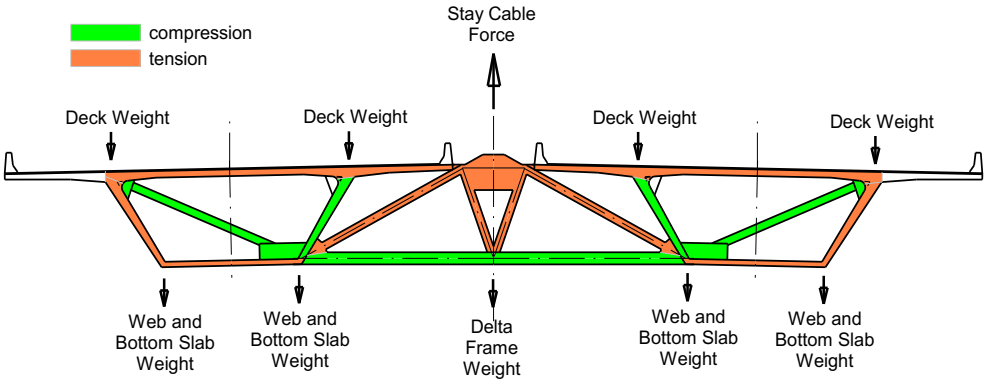

Figure 1-3 Simple Truss Model of Boxes and Delta Frame for Dead Load Only (Wollmann & Koutronamos, 2017)

The Varina-Enon Bridge has a history of corrosion related issues. For instance, two tendons in the approach spans have failed and at least one of the transverse tendons in the cable supported spans has broken. In addition, it has been observed that match cast joints open and close during traffic. This project will focus on the failure of transverse tendons. The transverse tendon break occurred in the back span close to the cable stayed spans. It

is unclear why the break occurred at this section of this bridge, so further studies are needed to determine this issue. For instance, the break could be random or related to poor grouting or it could be due to some aspects of structural behavior, such as high stress levels in this particular region. In addition, evidence shows the tendon break happened for a strand that was inside a not grouted duct. Figure 1-4 shows the location of the tendon break inside the Varina-Enon Bridge.

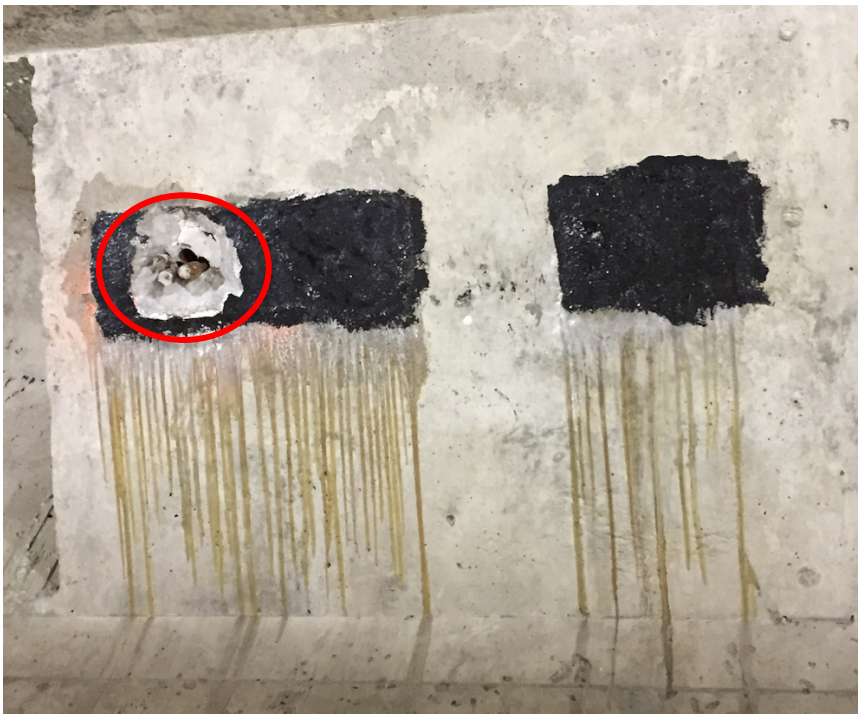

Figure 1-4 The Location of the Tendon break Inside the Varina-Enon Bridge

Also, in the Varina-Enon Bridge, inspectors have noted locations where it appears that the pour-back material in the block out pockets on the inside of the bridge has been dislodged, possibly due to strand fractures. Figure 1-5 shows the dislodged block out pocket on the inside of the Varina-Enon Bridge.

Figure 1-5 The Dislodged Block Out Pocket on the Inside of the Varina-Enon Bridge

1.3 Objective

This project has several objectives, which will help Virginia Department of Transportation (VDOT) to improve the performance of the Varina-Enon Bridge and they are listed below:

1. Investigate the consequences of transverse tendons rupture and the effect of failure in a well grouted or poorly grouted duct.

2. Identify if the bridge can perform adequately with no repair or if these failures would develop problems in the long term.

3. Provide information to support the future development and implementation of an instrumentation system to monitor the critical locations in the bridge.

1.4 Scope

The scope of this project is to use computer modeling and laboratory tests to address the issues related to transverse tendon breaks in the Varina-Enon Bridge. The objective of this project has been pursued by following tests:

1. Laboratory Specimens

   A post-tensioned slab with two tendons was built at the laboratory. The full scale specimen was built to contain tendons similar to top flange near the delta frames in the Varina-Enon Bridge, where the transverse tendon was broken. A smooth duct was used in the full scale specimen to mimic the ones used in the Varina-Enon Bridge. To analyze different scenarios two qualities of grouting were used for this specimen: one duct was well grouted and the other one poorly grouted. An accelerated corrosion process was used to corrode the tendons and investigate the effect of wire break on the slab. These tests provide additional information about tendons in the Varina Enon Bridge which are assumed to be broken due to damage seen at the anchorage pour backs.

2. Computer Model

   A finite element model was designed similar to the laboratory specimen to compare the collected data with the data obtained from the analysis. Also, the finite element model provided more information in order to have a better understanding of the behavior of the full scale specimen.

3. Instrumentation

   The specimen was instrumented with BDI strain gauges to monitor the behavior of the specimen when the strand rupture occurred due to the accelerated corrosion.

Changes in strain along the length of the specimen provided information about how well the strands were bonded to the duct and the duct to the concrete.

The dead end anchor, farthest from the location of the corrosion, was carefully monitored using LVDT sensors. The LVDT sensors tried to capture the movements of pour-back material in the block out pockets.

2. LITERATURE REVIEW

This chapter represents previous relevant research, including laboratory testing of corroded post-tensioned beams, the effect of potentially inadequate grouting quality on the performance of post-tensioned beams, and the detection and evaluation of failure of tendons.

2.1 Laboratory Testing of Corroded Post-Tensioned Beams

A number of previous experimental studies have investigated the mechanical response of post-tensioned beams after the artificial corrosion in the strands.

In research by Castel et al. (2012), the focus was to investigate the effect of tendon breaks from artificial corrosion. Five post-tensioned beams, each with one seven-wire strand, were built at the lab. Beams PC3 and PC2 were subjected to artificial corrosion, in which a reservoir was filled with NaCl and water solution and the corrosion location was anodically polarized to 10V. The corrosion process was conducted until the number of broken wires were visually observed. In addition, a Macro finite element (MFE) model was used to verify the data obtained by the laboratory tests. The MFE model was a beam characterized by homogenized inertia, and it considered the effect of prestressing force in the prestressed concrete with bonded tendons.

Figure 2-1 is a comparison of MFE simulation and experimental results for beam PC3. The graphs show separate curves for the MFE model after 30%, 60% and 100% steel corrosion reduction. In Figure 2-1, the experimental curve matches the 30% steel cross section reduction until it reaches the first wire failure. After that, the 60% cross section reduction follows the experimental curve until the second wire failure, and at the end when all of the wires are broken, the curve almost corresponds to reinforced concrete behavior. That shows the changes in the behavior of the prestressed concrete as the strands are losing strength and failing.

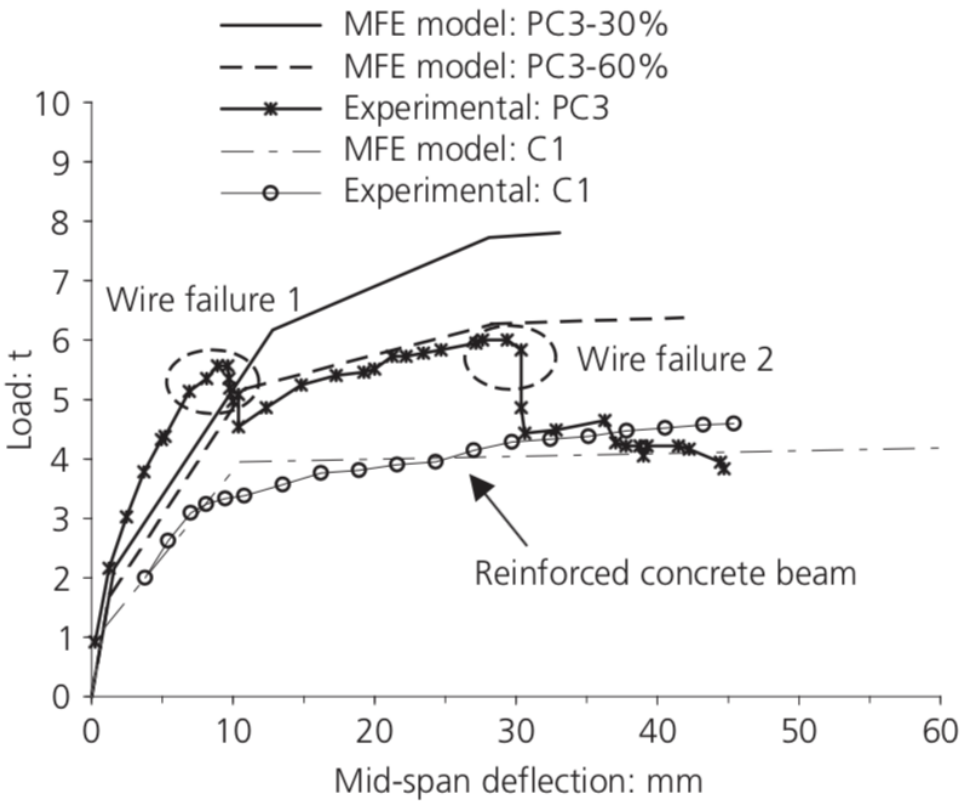

Figure 2-1 Comparison of MFE Simulation and Experimental Results for Beam PC3 (Castel et al., 2012)

The MFE model matched laboratory test very closely, however they were slightly different because the model designed with the limited knowledge of materials properties and post-cracking stiffness.

In the research presented by Coronelli et al. (2009), post-tensioned specimens with bonded wires were built at the lab and the effect of stress corrosion failure of the wire was studied. To cover all possible outcomes, wire failure was conducted in different locations. The effect of the wire failure depends on the position of the break with respect to the flexural load effect. For instance, in the case with the wire break close to the support, after the wire failure, the rest of the prestressing tendon can still provide the adequate resisting load effect, and the wire break does not affect the beam's strength and stiffness. On the other hand, wire failure between

load and support can cause a significant reduction in the capacity of the beam because the prestressing is nearly lost.

In addition, wire failure will cause local damage in areas closest to the broken wire, the cracking of the concrete is an apparent result of this. All of these indications are very helpful because they can provide guidelines in the existing structures that are experiencing tendon failure. Monitoring the structures with the knowledge obtained from laboratory tests is very important and can make a significant change in the rehabilitation methods and future studies.

In the research conducted by Zhang et al. (2017), the objective was to investigate the flexural behavior of post-tensioned beams subjected to artificial corrosion. The corrosion in tendons has less effect on the yield strength and elastic modulus, however it reduces the ultimate strain of the strand and leads to brittle failure. Cracking of the beam depends on the corrosion level, for instance, the corrosion increases the cracking space but decreases the number of cracks. In addition, corrosion in tendons decreased the ultimate strength of the concrete and changes the failure mode. Therefore, the wire rupture will occur before concrete crushing.

2.2 Grouting in Post-tensioned Beams

Insufficient grouting will reduce protection of strands from de-icing salt, salt fog and rainwater. Therefore, not having good protection will accelerate the corrosion rate of strand and result in strand failure. Consequently, sufficient grouting used as protection for the prestressed strands and without it, the strands are very vulnerable to corrosion. In addition, corrosion of a strand subjected to high stress can cause many problems such as decrease in tensile capacity and ductility of the strands.

In research conducted by Wang et al. (2013), the objective was to investigate the effect of insufficient grouting-induced strand corrosion on the flexural behavior of post-tensioned concrete beams. Five post tensioned beams with different grouting conditions were built at the lab and were subject to loading. The result of these five post-tensioned beams showed the crack distribution and crack width depend on qualities of grouting and the ungrouted length and position. Figure 2-2 shows the typical load-deflection curves for the beams

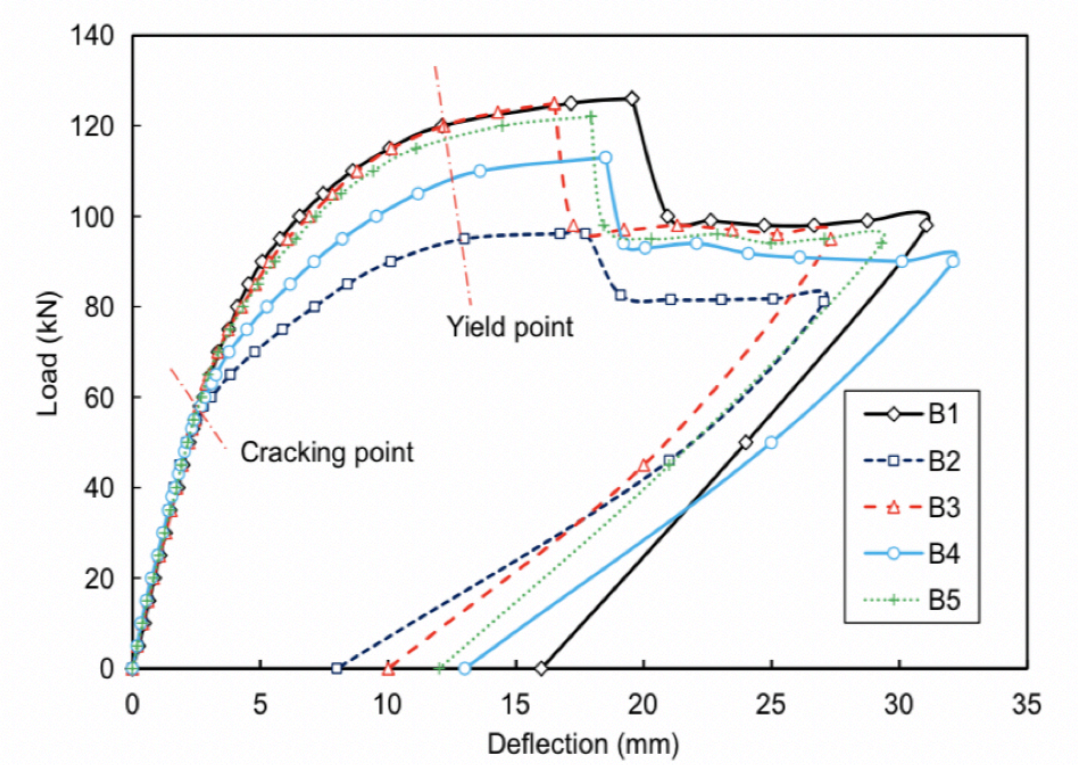

Full grouting (B1), No grouting (B2), Grouting in only half of the duct cross-section (B3), No grouting in the half span (B4) , No grouting in the central region (B5).

Figure 2-2 Load-Deflection Curves (Wang et al., 2013)

Before the cracking point, all the beams have same load-deflection behavior. However, insufficient grouting, the ungrouted length and position affect the post-cracking stiffness and the

ultimate strength. The insufficient grouting decreases stiffness of the beam and the ultimate strength significantly. Therefore, everything related to grouting such as grouting ratio, ungrouted duct length and location ultimately affect the strength of the beam.

In addition to sufficient grouting, the quality of the grout in the ducts is very important in post-tensioned bridges. The research presented by Kamalakannan et al. (2018), discussed the characteristics of good grout and how the bad quality grout can result in premature failure of tendons. In order to protect the post-tensioned strand in the long term, the duct needs to be completely filled with a good quality grout. In addition, the quality of the grout is affected by ambient temperature, the mixing speed and the fineness. For instance, a change in the ambient temperature from 15-30 ^{o}C can affect the bleeding resistance of the grout.

Evaluating the grouting condition is very important in health monitoring of post-tensioned bridges. In the research conducted by Cheong et al. (2018), grouting condition was evaluated using the Rayleigh wave (R-wave). The concept of evaluating the grouting condition is based on the fact that R-waves experiences different frequencies as they propagate through different qualities of grouting. For instance, the wave velocity is slower when it travels through grouting with voids, and the grout with voids has a higher frequency. This method is very effective, and it has been used in several bridges that are in service.

2.3 Detecting Wire Break in Corroded Post-Tensioned Beams

Acoustic emission (AE) is a technique to measure elastic waves generated by sudden changes, which occur locally in materials due to deformation, cracking, transformation and so

forth. Since AE systems are very sensitive and can detect cracking and failure in the material, they are widely used to detect failures in prestressed concrete structures. AE is very useful to locate cracking in reinforced concrete structures and in order to detect cracking in prestressed concrete structures, the AE system must be modified. For instance, AE systems need to be characterized for the elastic waves produced by wire breaks, and to detect the source location for the wire breaks. AE analysis systems are based on hit, count, amplitude, energy, rise time, and duration to detect and locate wire breaks. Also, AE systems need to consider the effects of traffic noises and be able to detect the wire breaks under very noisy environments due to traffic.

In research conducted by Yuyama et al. (2006), laboratory tests were conducted to investigate the effectiveness of AE systems. Three post-tensioned beams with a steel bar, a 12 wire strand, and a 12 wire parallel-wire cable were built at the laboratory, and each beam had three different grouting conditions: ungrouted, partially grouted and fully grout. The beams contained an 18 channel AE system and an 8 channel digital AE system and AE monitoring was performed continuously for 3 weeks. Also, an accelerated corrosion process was conducted to corrode the tendons. The successful ratio of detected wire breaks in beams with a 12 wire strand (B2), and a parallel 12 wire strand cable (B3) were 82% and 86%, respectfully. Figure 2-3 and Figure 2-4 show the locations of all the events detected by AE system in beams B2 and B3, respectively. As shown in the figures, the AE system is an effective method to detect wire failures.

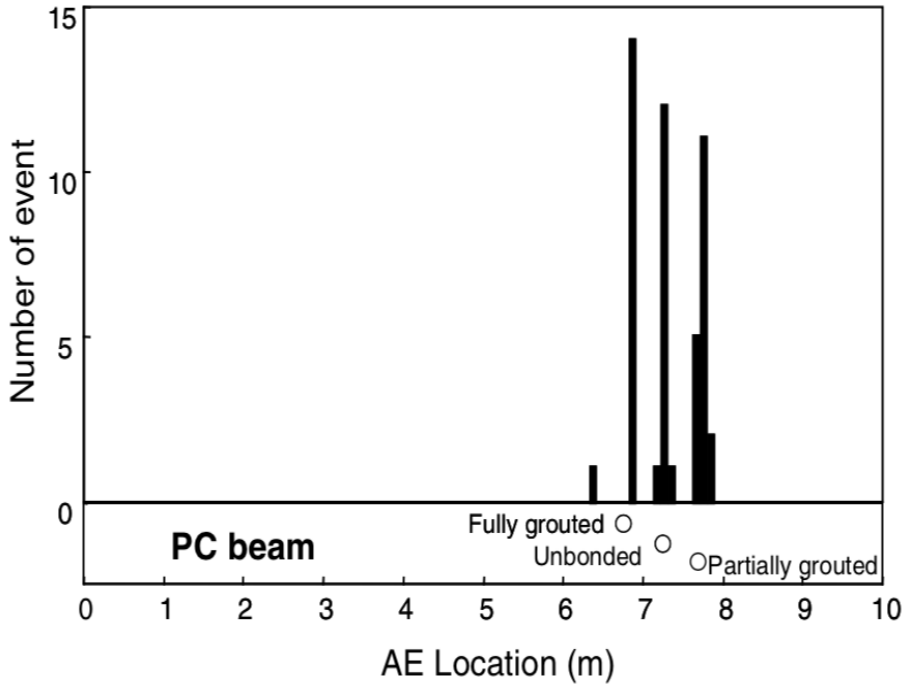

Figure 2-3 Location of all the Events Detected by AE in the B2 Beam (Yuyama et al., 2006)

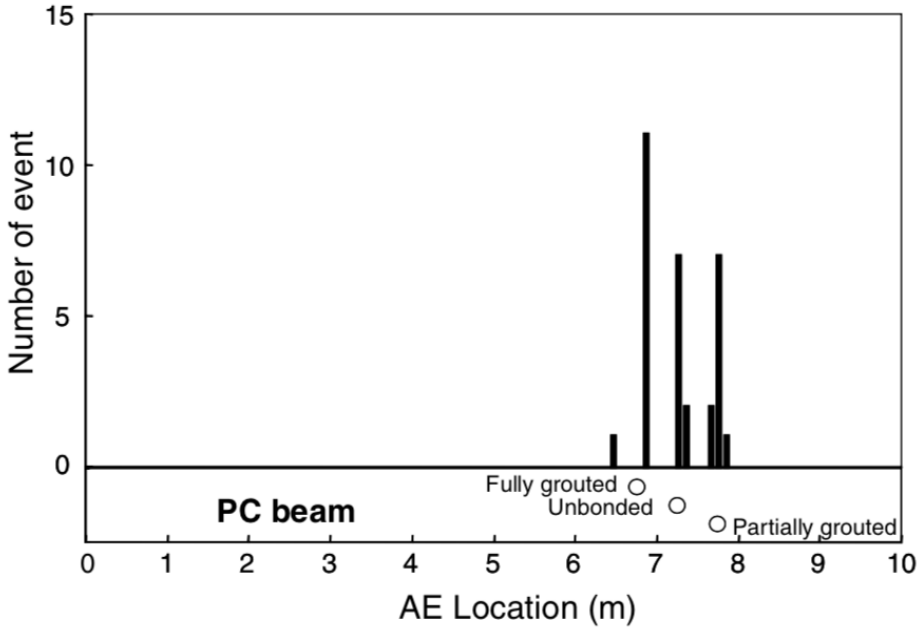

Figure 2-4 Location of all the Events Detected by AE in the B3 Beam (Yuyama et al., 2006)

Furthermore, in the research presented by Fricker and Vogel (2006), an AE monitoring system was installed on a post-tensioned bridge in Switzerland. The goal was to use AE

monitoring as a non-destructive method to detect and investigate the wire breaks in this bridge. An AE system was installed along the bridge and they were able to detect several spontaneous wire breaks. Based on the characteristic of different signals, the wire breaks occurred in a partially grouted tendon. For this bridge, three of the spontaneous wire breaks were confirmed by an invasive inspection. The AE monitoring is a promising way to detect the wire breaks and was able to record, classify and locate wire breaks in grouted and partially grouted tendons.

Another approach to identify wire breaks in post-tensioned bridges is by using strain gauges. In post-tensioned bridges, the anchors are under high prestressing forces and a wire failure results in change in the strain distribution of the anchor. Therefore, in research conducted by Abdullah et al. (2016), the strain gauges were attached on the circumferential perimeter of an anchor to detect wire breaks. (Figure 2-5). The way to identify the broken strand is that part of the anchor head at the location of the broken strand experiences larger strain relief compared to other regions. The instrumentation plan proposed by this author is very effective to detect wire breaks in the full-scale specimen at the laboratory. However, in-field instrumentation and testing are needed before this method can be widely implemented.

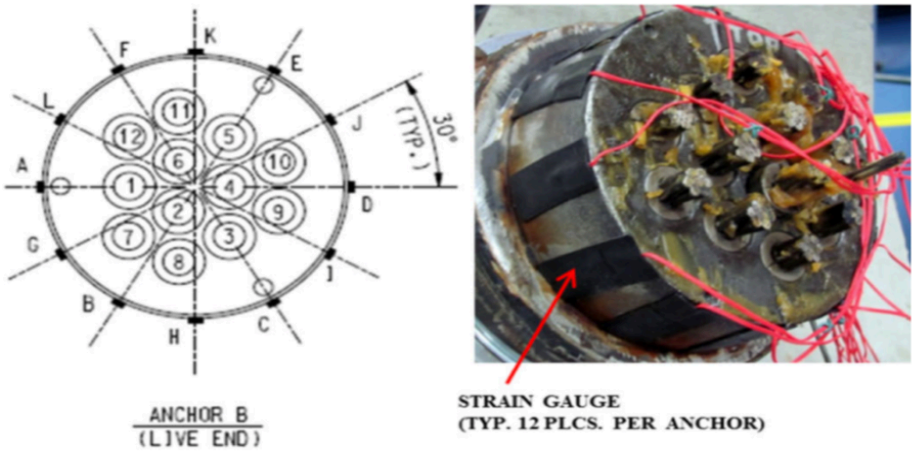

Figure 2-5 Anchor instrumentation (Abdullah et al., 2016)

An alternative approach to detect corrosion and fracture in tendons in prestressed concrete is using an electromagnetic sensor system. In research by Fernandes et al. (2012), electromagnetic sensor systems were used to determine the effective cross-sectional area of the prestressing strands. Therefore, this method can detect the material loss due to corrosion which is not possible from the surface inspection. In addition, the author proposed that the electromagnetic sensor systems can be improved by changing the arrangement of the sensors or the magnet design. Although the electromagnetic sensor system is very effective to detect corrosion in the strand, it has some risks. For instance, interfering the magnetic readings with the corrosion product or the water in the corrosion product.

3. METHODOLOGY

This chapter presents an overview of the methods that have been employed to investigate the issues related to transverse tendon breaks. These methods consist of the followings:

1. Accelerated Corrosion Test
2. Laboratory Specimens
    a. Small Specimen
    b. Full Scale Specimen
3. Computer Model

3.1 Accelerated Corrosion Tests

The purpose of the corrosion test was to find the fastest method to artificially corrode the tendons. The chosen method was later used in the laboratory specimens to corrode the tendons after they have been stressed. Small pieces of 0.5 in. diameter prestressing strand (about 2 in. long) were submerged in three different solutions: salt and vinegar, salt and water (saline solution) and household bleach. Each specimen went through the following process everyday: The specimen was removed from the solution and left out to be dried. Afterwards it was weighed and then returned to the solution. All the specimens started corroding after 2-3 days, but results show that the ones in bleach and saline solution corroded at a much faster pace and started experiencing some mass loss. Figure 3-1 shows a specimen before and after it has been submerged in saline solution for ten days.

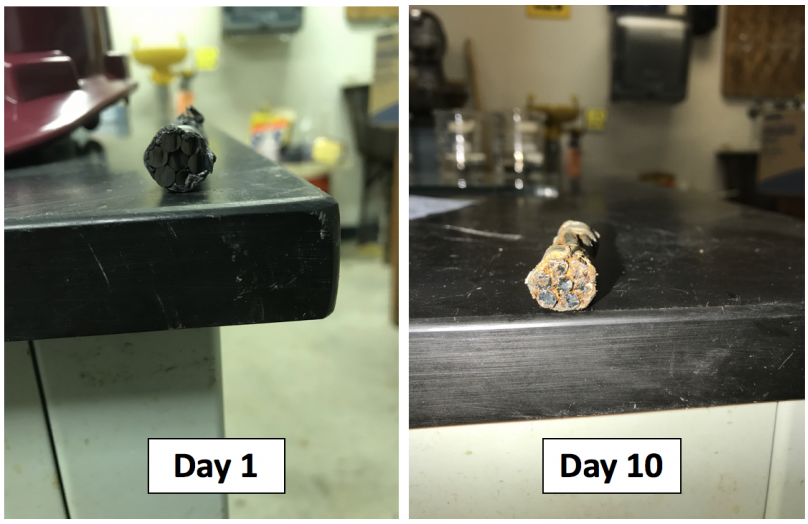

Figure 3-1 A Tendon Specimen Before and After Being Submerged in Saline Solution for 10 Days

Results show that household bleach was the most effective solution to corrode the tendons. The specimens in bleach experienced 3% mass loss after seven days and 5.7% after fourteen days respectively. Figure 3-2 represents a graph of mass loss over time for the specimens submerged in all three solutions.

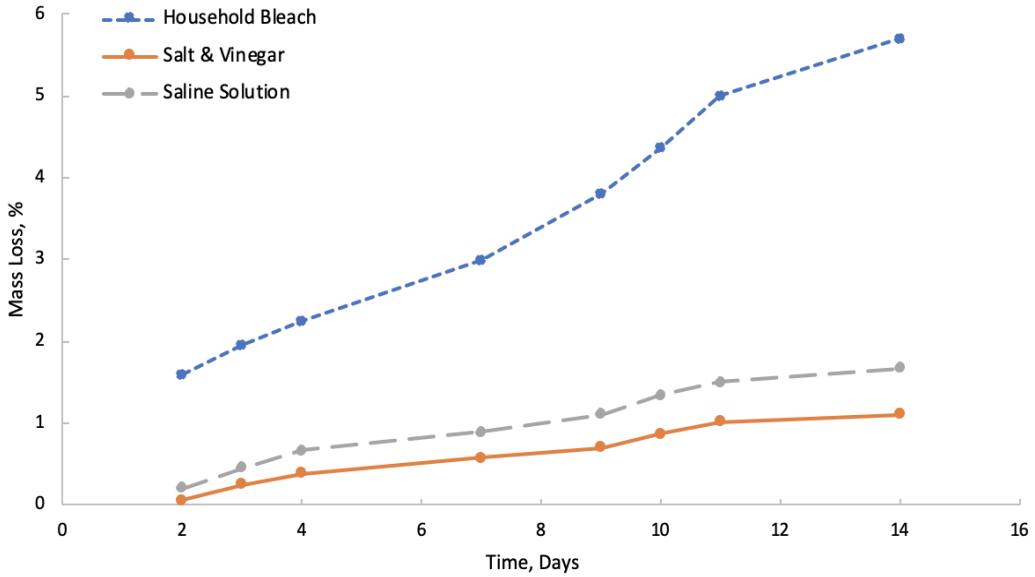

Figure 3-2 Mass Loss vs. Time Graph for Specimens Submerged in Bleach

As shown in Figure 3-2, the mass loss percentage for the specimens in salt and vinegar and salt and water are very small compared to the one in the household bleach. In addition, Figure 3-3 shows a specimen before and after it has been submerged in bleach for seven and fourteen days.

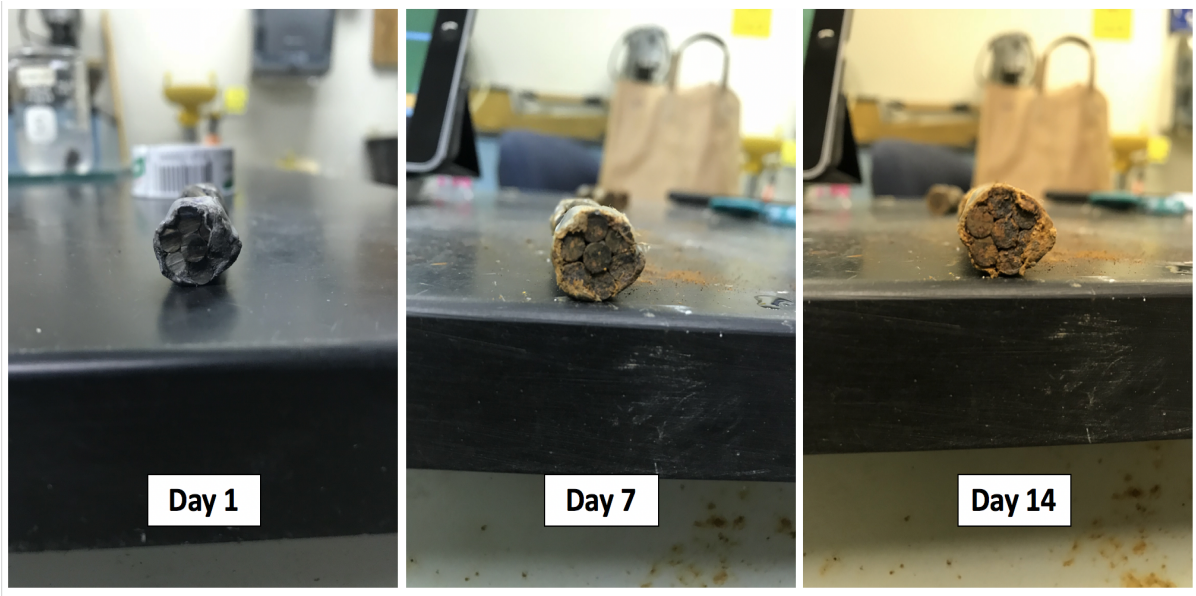

Figure 3-3 A Tendon Specimen Before and After Being Submerged in Bleach for 7 and 14 Days

As discussed in the Chapter 2, one of the common methods to accelerate the corrosion rate of tendons in the laboratory was reverse cathodic protection. After finding the best solution to corrode the tendons, consideration was given to combining this method with a reverse cathodic protection. Submerging the strands in household bleach and putting an electric current through it will produce dangerous chlorine gas. Therefore, instead of using household bleach and electric current, saline solution was used along with the reverse cathodic protection in the laboratory specimens.

3.2 Laboratory Specimens

Laboratory specimens were built in the Murray Structures Laboratory at Virginia Tech to provide additional information about tendons in the Varina-Enon Bridge, which are assumed to be broken. The purpose of the following tests was to build specimens to recreate the conditions within the section of the Varina-Enon Bridge that is currently experiencing problems.

3.2.1 Small Specimen

The main purpose of the small specimen was to estimate the time needed to break the tendons by using both methods combined: submerging in saline solution and reverse cathodic protection. A 4 ft by 10 ft slab with thickness of 8 in. was built at the lab. The slab was constructed with 0.5 in. diameter strands at 10 in. spacing and each tendon was in a 1 in. by 2 in. corrugated plastic duct. Figure 3-4 shows the drawing of elevation view and plan view of the small specimen.

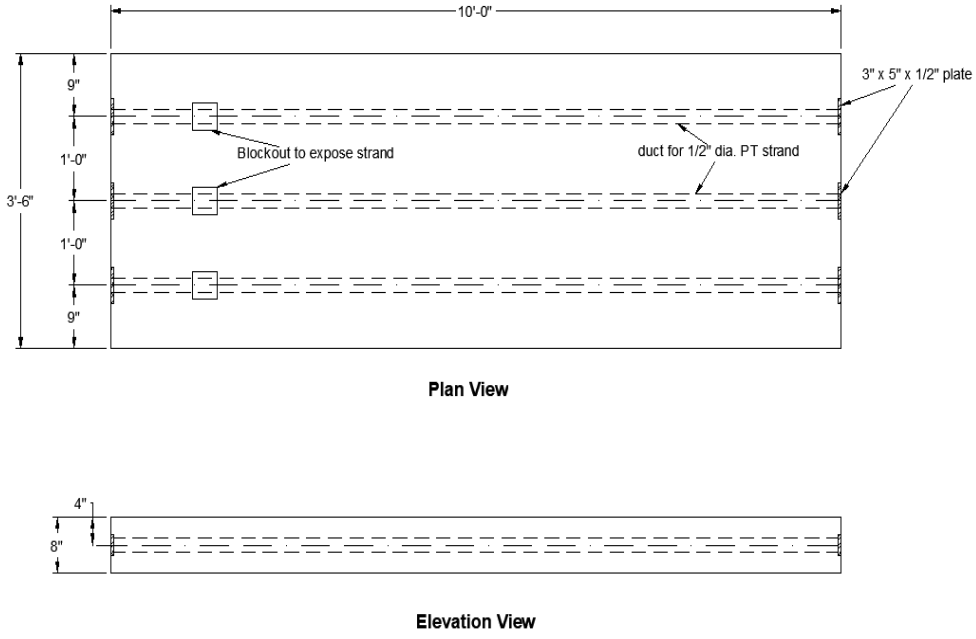

Figure 3-4 Drawing of Plan View and Elevation View of the Small Specimen

In addition, black plastic tubes were attached to allow the pumping of the grout inside the ducts. Minimum reinforcement was placed in the slab for handling. Transverse reinforcements that consisted of No. 3 bars with 15 in. spacing and No. 4 bars with 15 in. spacing were used for longitudinal reinforcements. Figure 3-5 shows the transverse and longitudinal reinforcement and the ducts and grout tubes in the slab.

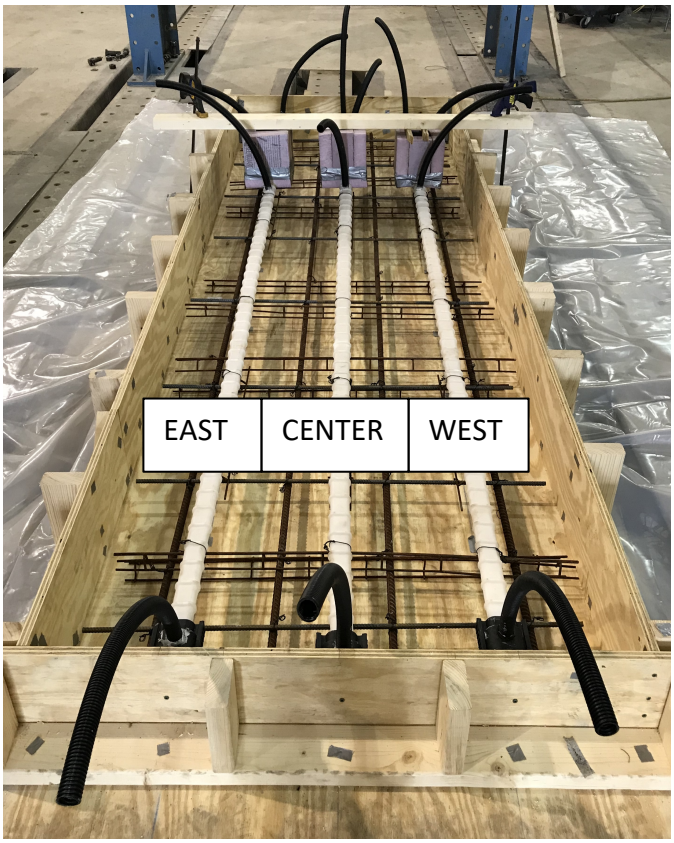

Figure 3-5 Transverse and Longitudinal Reinforcement, the Ducts and Grout Tubes

There were block-outs over each duct to allow access to tendons for corrosion purposes. After placing concrete, the block outs were taken out and the ducts were cut off so the strands would be exposed for the corrosion test. Figure 3-6 shows the slab after the concrete was placed. In addition, Figure 3-7 shows a clear view of the inside of the block out after the duct was cut off.

Figure 3-6 The Slab After Concrete was Placed

Figure 3-7 A View of the Block Out After the Duct was Cut Off

Each tendon was stressed to 75% of its guaranteed tensile strength, which is 202.5 ksi, or 30.8 kips per strand. Also, each tendon was stressed separately by using a small hand pump and small center-hole ram with an elongation capacity of 1.5 in. The theoretical elongation for each tendon was calculated to be 1.0 in. after stressing. Each tendon was stressed incrementally (every 6 kips) to reach the jacking force and in each stage, the total elongation, the dead end seat and ram wedge seat were measured. Table 3-1 shows the prestressing data collected for small specimen. The calculated net elongation for center, west and east tendon are 0.81 in., 0.97 in. and 0.81 in. respectively. Table 3-2 shows the elongation results for small specimen. The net elongation was less than the theoretical value due to the curvature and wobble friction. Also, the percent error between the net value and the theoretical value is presented in Table 3-2. In addition, Appendix A shows the calculations for the theoretical and net elongation.

Table 3-1 Prestressing Data for Small Specimen

Load (kip)	Displacement (in)		
	Center	West	East
6	1.00	1.00	1.25
12	1.25	1.25	1.63
18	1.50	1.56	1.88
24	1.75	1.88	2.06
31	2.06	2.19	2.31
Dead end seat (in)	0.13		
Ram wedge seat (in)	0.13		

Table 3-2 The Elongation Results for Small Specimen

Elongations	Center	West	East
Factored Elongation (in)	1.32	1.47	1.32
Dead end seat (in)	0.13	0.13	0.13
Ram wedge seat (in)	0.13	0.13	0.13
Elongation in ram (in)	0.26	0.26	0.26
Net elongation (in)	0.81	0.97	0.81
Theoretical Elongation (in)	1	1	1
Percent error %	18.84	3.34	18.84

The ducts at the block outs were plugged by using a spray foam to prevent grout entering the block outs. The grouting process was conducted by attaching the black tubes in the slab to the grouting tube. The grout that was used for this specimen had a water-cement ratio of 0.45, which represents a good grout. Figure 3-8 shows the grout pump and grout tube connected to the plastic tube during the grouting process.

Figure 3-8 Grouting Process

After stressing and grouting the tendons, the corrosion process was started. Corrosion process was conducted by submerging the tendon in a liquid and putting an electric current through. Each block out was filled with saline solution (5% salt) and a current intensity of 0.3 Amps was applied. In order to corrode the strand, the strand needed to go through an oxidation process by losing electrons. Therefore, an outside source (current intensity) was needed to take electrons from the strand. By connecting the strand to the positive side, the electrons would leave the strands and strand will go through an oxidation process. Therefore, the strand was the anode, while a steel plate submerged in the saline solution was the cathode. Electrons flowed from strand (anode) to steel plate (cathode) and that was how the strands inside the block out start to corrode. Figure 3-9 shows the drawing of the experimental setup in detail, and Figure 3-10 shows a block out and the steel bar (cathode) during the corrosion experiment.

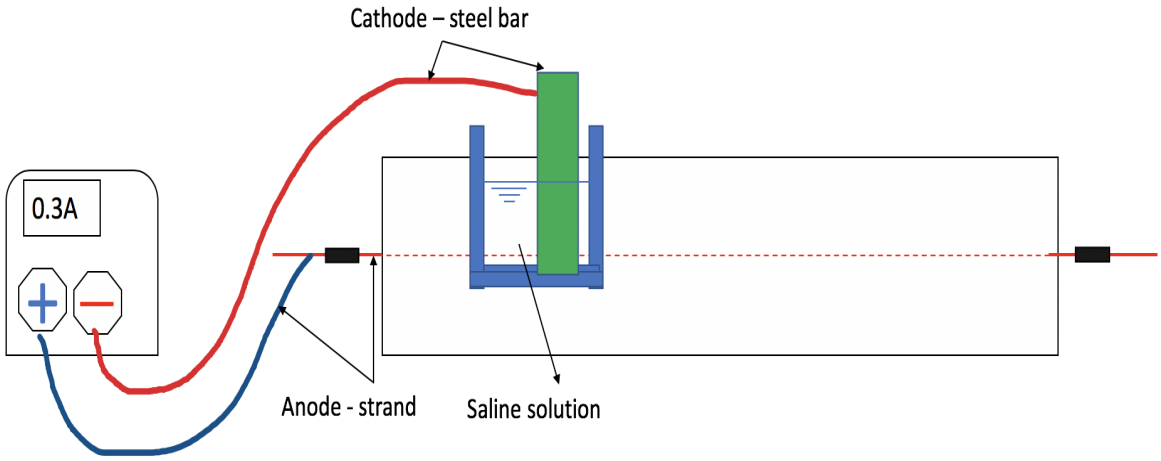

Figure 3-9 Drawing of Corrosion Experiment in Detail

Figure 3-10 The Block Out During the Corrosion Experiment

The corrosion process was conducted six hours per day for a total of three days, and at the end of each day, the saline solution was removed from the block out and pictures were taken to record all the changes in the strand condition. The tendon was fully corroded after three days, and it was fully dissolved in the saline solution. This process was repeated for all three block outs and the result was similar for all tendons and they were broken after 3 days. Figure 3-11 presents the progress in the strand corrosion process over three days. This artificial corrosion developed localized corrosion in the strands and proved to be an effective method to corrode the tendons. By using this method, the tendons will reach the desired condition and break.

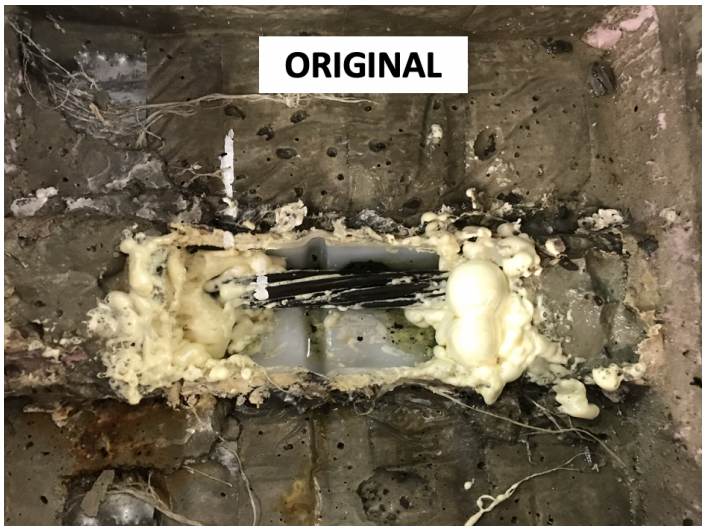

a)

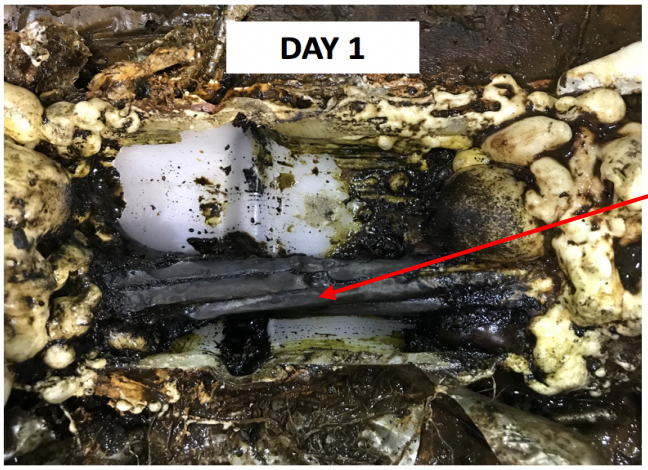

b)

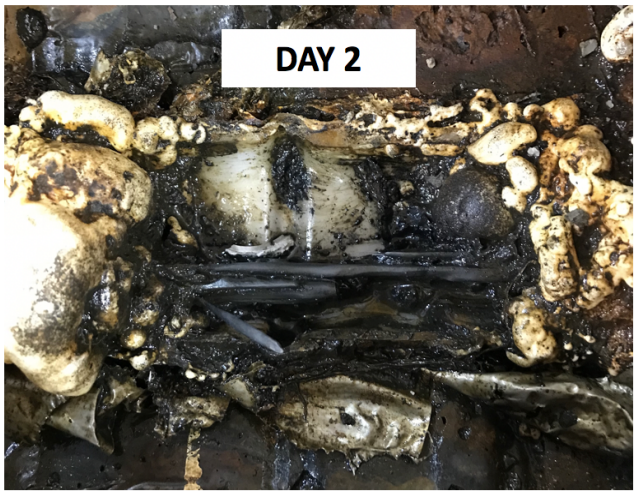

c)

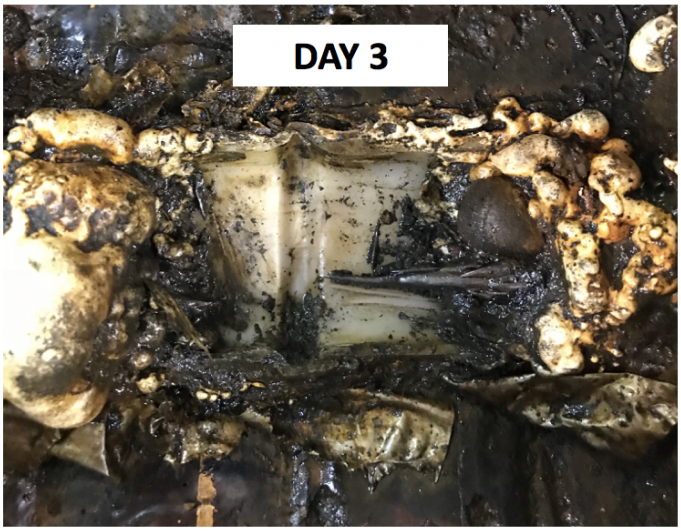

d)

Figure 3-11 Progress in the West Strand Corrosion Over Three Days

3.2.2 Full Scale Specimen

The full scale specimen was built to contain tendons similar to top flange near the delta frames in the Varina-Enon Bridge, where the transverse tendon was broken. The slab was 3 ft – 4 in wide and 75 ft long with 9 in. thickness, and there were two 1in. by 3 in. smooth flat plastic ducts with 20 in in between each duct. In each duct there were four 0.6 in. diameter strands, similar to those used in the Varina-Enon Bridge. In addition, a 7 ft section with a thickness of 3 ft. was built at the end of the slab so the ducts curve up to match the Varina-Enon Bridge plans. Figure 3-12 shows a drawing of the full scale specimen. Also, Figure 3-13 shows the transverse frame in the Varina-Enon Bridge and the red line presents the transverse tendon path. As shown in the Figures below, the tendon path for the full scale specimen was designed to match the transverse tendon path in Varina-Enon Bridge.

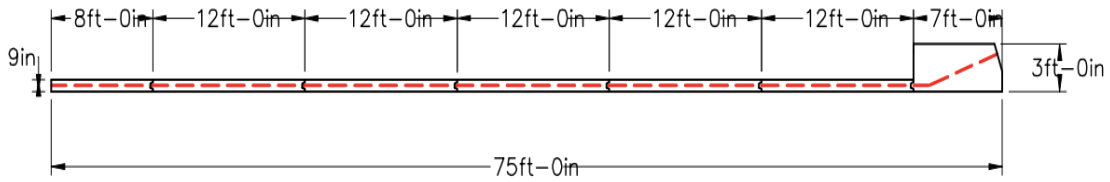

Figure 3-12 A Drawing of the Full Scale specimen

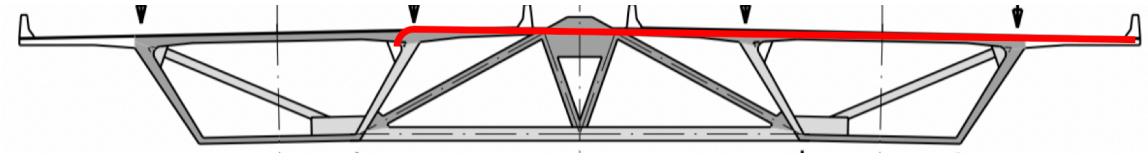

Figure 3-13 A Tendon Path for a Transverse Tendon in the Varina-Enon Bridge

Figure 3-14 shows a drawing of tendon path at the end section and how the tendons curved up to match the transverse tendon in the Varina-Enon Bridge.

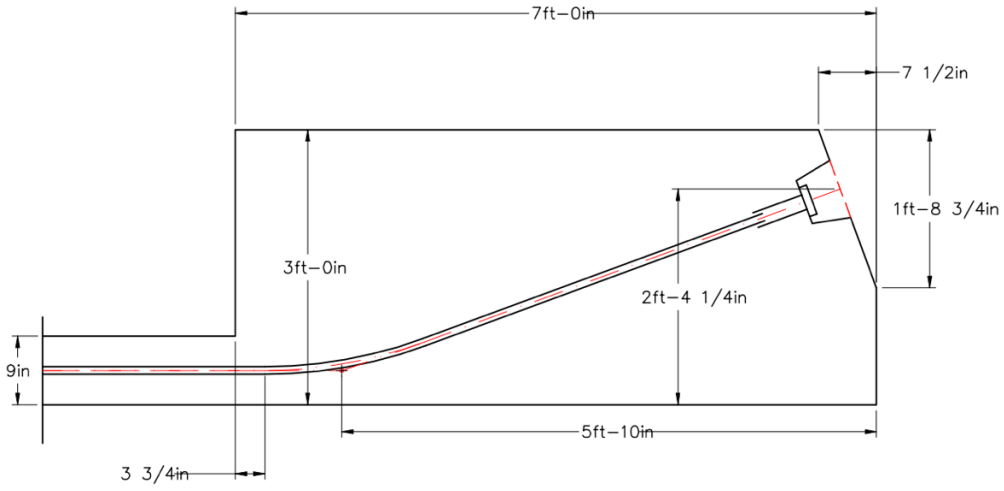

Figure 3-14 Tendon Path at the End Section

Figure 3-15 shows the smooth flat duct that was used in the full scale specimen to mimic the ones used in the Varina-Enon Bridge.

Figure 3-15 View of the Smooth Duct

The full scale specimen was divided into several smaller sections for the eases of demolition process when the project was done. The slab consists of one 8 ft section, five 12 ft sections and a 7 ft section at the end. Figure 3-16 shows a drawing how the slab was divided into different sections.

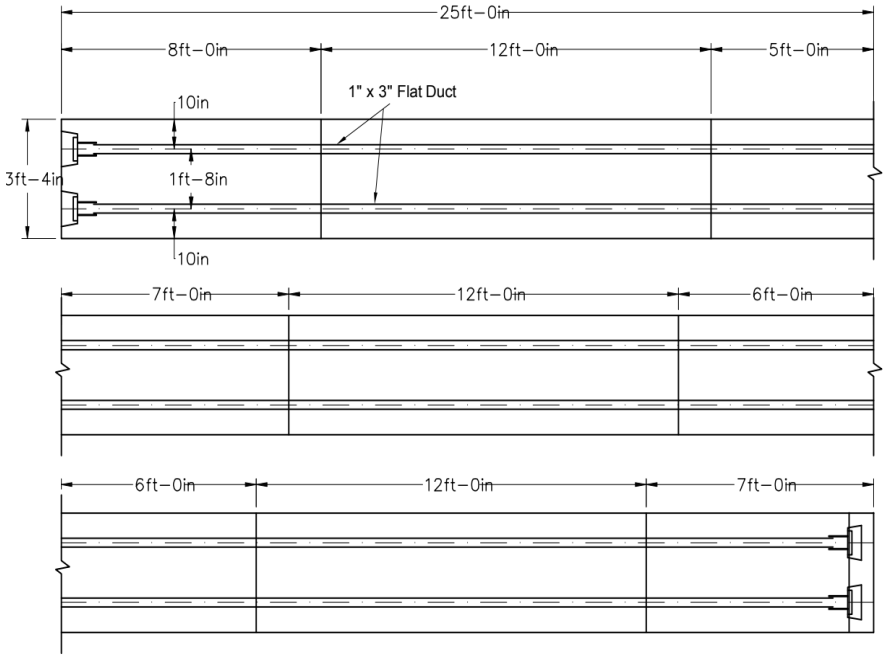

Figure 3-16 Drawing of the Full Scale Specimen Divided into Different Sections

Minimum reinforcement was placed in the slab for handling and to control cracking in the concrete. No. 4 bars with 15 in. spacing were used for both transverse and longitudinal reinforcement, and the end section contains of No. 4 hoops.

Sixteen block outs were built into this specimen: two for corrosion purposes and 14 for the ease of the demolition process. Figure 3-17 shows transverse and longitudinal reinforcement and the ducts before placing the concrete. Figure 3-18 shows the reinforcement in the end section.

Figure 3-17 Transverse and Longitudinal Reinforcement and the Ducts

Figure 3-18 Reinforcement at the End Section

The slab was casted in two stages for the ease of the demolition process and bulkheads with shear keys were used to separate the sections from each other. In order for the bulkheads to be disconnected from each section after the first cast, a mixture of talc and liquid soap was used as the bond breaker. After each cast, concrete cylinders were made, and they were tested in order to measure the strength and the modules of elasticity of the concrete. Figure 3-19 shows the full scale specimen in the both stages of casting.

a) Casting Stage 1

b) Casting Stage 2

Figure 3-19 Casting Process

All the pieces of the full scale specimen were designed to recreate the Varina-Enon Bridge. For instance, the anchor plates were designed similar to the plates that were used in the Varina-Enon Bridge. However, the hole locations needed to be altered to accommodate the chuck bodies. Figure 3-20 a shows the drawing of the anchor plates that were used in in the Varina-Enon Bridge and Figure 3-20 b shows the modified drawing of the anchor plate that was designed for full scale specimen.

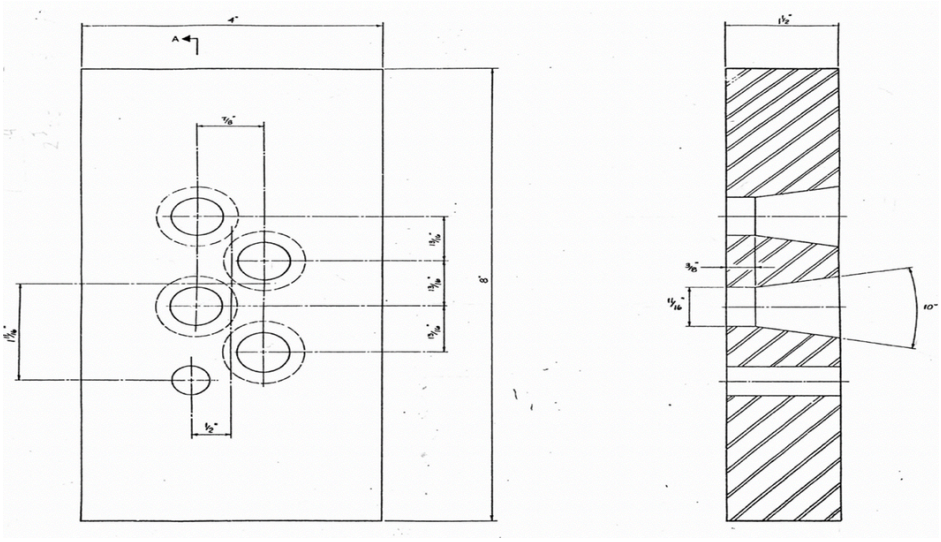

a) Drawing of the Anchor Plate for Varina-Enon Bridge

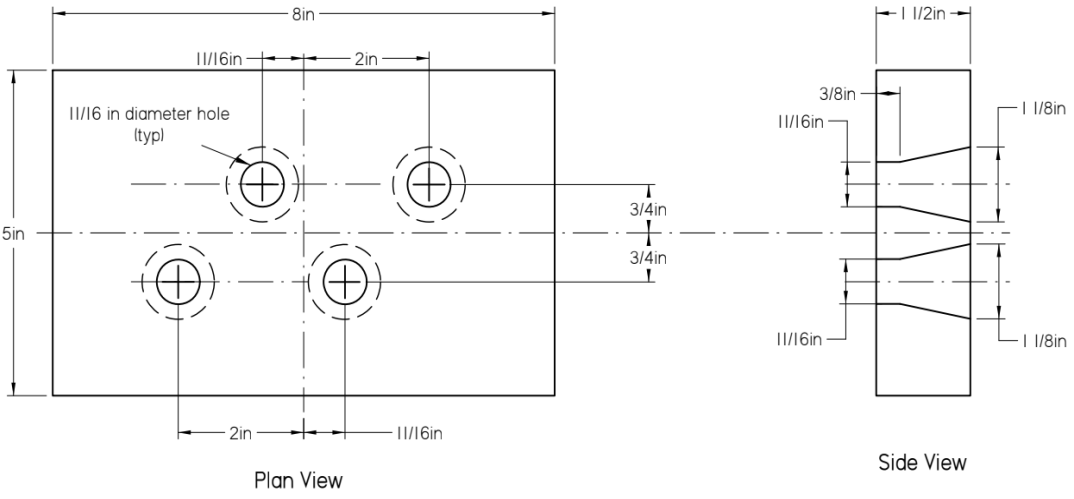

b) Modified Drawing of the Anchor Plate for Full Scale Specimen

Figure 3-20 Anchor Plates

In order to obtain data from the lab experiment, different types of instrumentation were installed on the slab. BDI strain gauges were used to measure the strain in the concrete during the stressing process. In addition, they were used to capture any unusual strain change in the concrete once the tendons broke. There were six BDI strain gauges along each tendon (12 in total) and four of them were close to the corrosion block out, one in the middle and one close to the end section. Figure 3-21 shows a plan view of the slab with the locations of the BDI strain gauges.

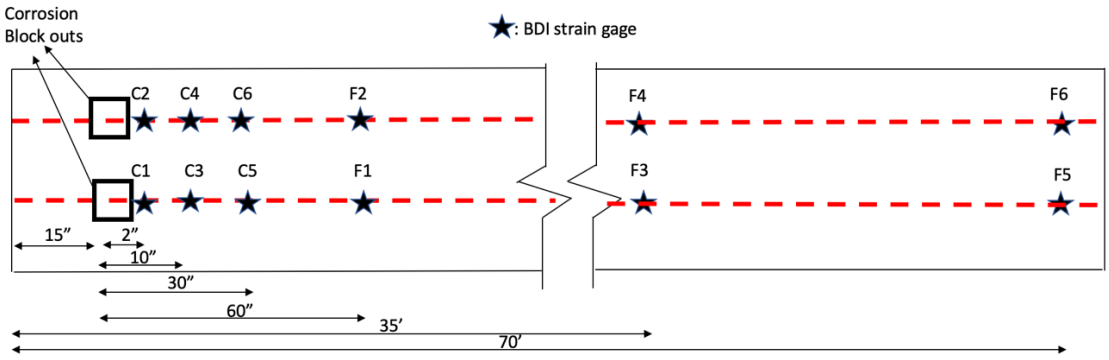

Figure 3-21 Locations of the BDI Strain Gauges on the Full Scale Slab

In addition, pour-back material in the block out pockets on the inside of the Varina-Enon Bridge have been dislodged, possibly due to strand fractures. So, LVDT sensors were installed in the full scale specimen on the pour-backs at anchorage block-outs to determine if any movement at the pour-backs occurred. Figure 3-22 shows the pour-back material in the block out pockets.

Figure 3-22 The Pour-Back Material in the Block Out Pockets

In the full scale specimen, the tendons were stressed to a lower jacking stress (less than 75% of ultimate). Each tendon was stressed to 65% of its guaranteed tensile strength, which is 175.5 ksi, or 38 kips per strand.

Each tendon was stressed separately by using a hand pump. Figure 3-23 shows a detailed drawing and the actual set-up during the stressing process.

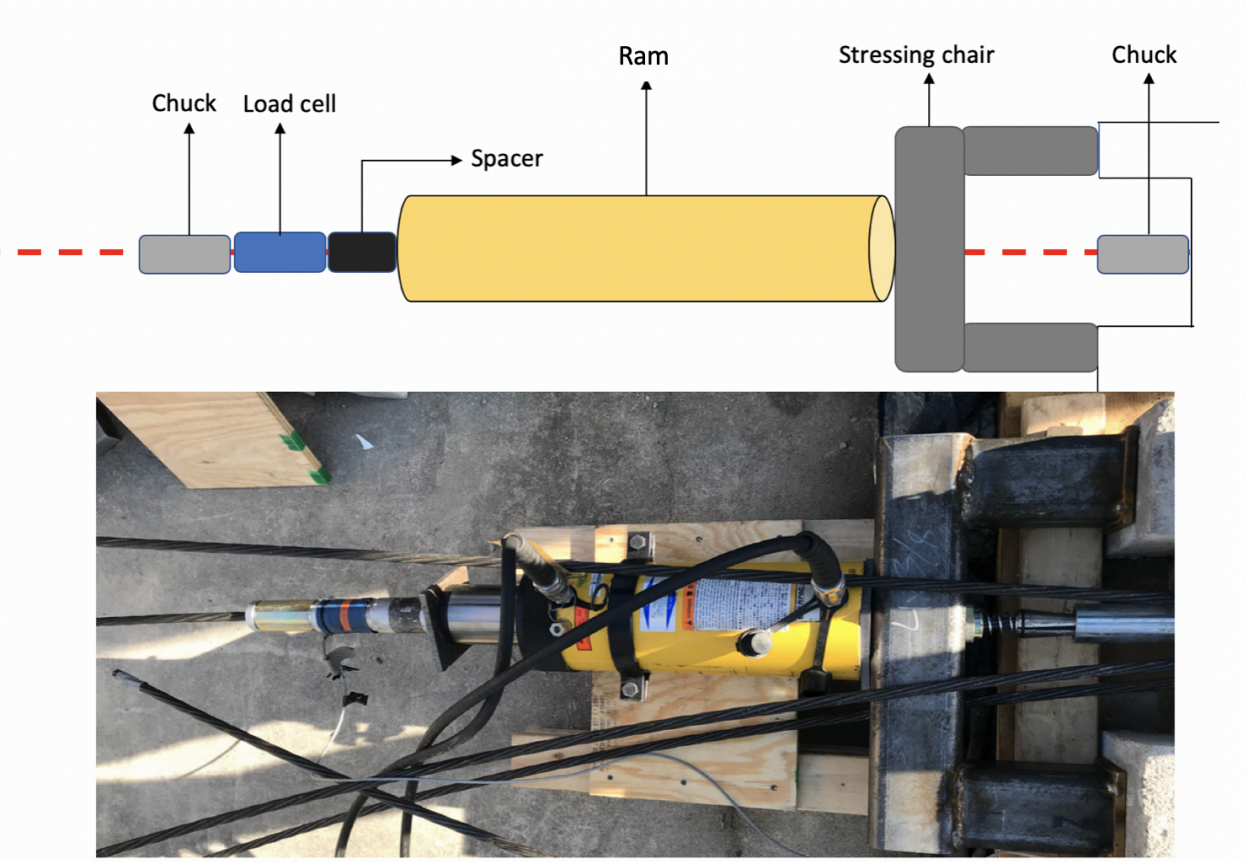

Figure 3-23 Detailed Drawing and the Actual Set-up During the Stressing Process

Each tendon was stressed separately by using a hand pump and center-hole ram with an elongation capacity of 7 in. The theoretical elongation for each tendon was calculated to be 5.46 in. after stressing. Each tendon was stressed incrementally (every 8 kips) to reach the jacking force and in each stage, the total elongation, the dead end seat and ram wedge seat were measured. Table 3-3 shows the prestressing data collected for full scale specimen. Also, Table 3-4 shows the elongation results for full scale specimen. The net elongation was less than the theoretical value due to the curvature and wobble friction. Also, the percent error between the net value and the theoretical value is presented in Table 3-4. In addition, Appendix A shows the calculation for the net elongation and the theoretical elongation.

Table 3-3 Prestressing Data for Full Scale Specimen

	Live end North				Live end South			
Load(kip)	1	2	3	4	1	2	3	4
4	5.00	4.38	5.00	5.94	3.13	4.19	4.75	4.81
14	6.56	5.81	6.63	7.38	5.00	5.75	6.38	6.38
22	7.81	7.00	7.94	8.88	6.19	6.88	7.56	7.50
30	8.88	8.13	9.19	9.06	7.44	8.13	8.81	8.63
38	10.00	9.25	10.50	10.63	8.69	9.38	10.06	9.81

Table 3-4 The Elongation Results for Small Specimen

Elongations	Live end North				Live end South			
	1	2	3	4	1	2	3	4
Factored Elongation (in)	5.59	5.45	6.15	5.34	6.22	5.80	5.94	5.59
Dead end seat (in)	0.13	0.13	0.13	0.13	0.13	0.13	0.13	0.13
Ram wedge seat (in)	0.75	0.50	0.50	0.50	0.38	0.31	1.50	0.50
Elongation in ram (in)	0.27	0.27	0.27	0.27	0.27	0.27	0.27	0.27
Net elongation (in)	4.44	4.55	5.25	4.44	5.45	5.09	4.04	4.69
Theoretical Elongation (in)	5.46	5.46	5.46	5.46	5.46	5.46	5.46	5.46
Percent error %	18.62	16.60	3.81	18.66	0.24	6.77	25.96	14.04

To analyze different scenarios and generate the most effective solution for the problem, two different qualities of grouting were used for this specimen: one duct was well grouted and the other one poorly grouted. The grouting process was conducted by attaching the black tubes in the slab to the grout pump. A water cement ratio of 0.45 was used for one duct which represents well grouted and the second duct was filled with a poor quality grout which had a water cement ratio of 0.65. Figure 3-24 shows two cylinders filled with different qualities of grout: a) good grout and b) poor quality grout.

a) b)

Figure 3-24 Cylinders Filled with Different Qualities of Grout

Both of the cylinders were filled fully with grout and were placed outside for two days. After two days, the water from the grout was evaporated and as shown in Figure 3-24, the cylinder with poor quality grout lost more volume due to the higher water cement ratio. In addition, the block out pockets at the end section were filled with very thick grout (paste) with a low water cement ratio of 0.15.

Based on ASTM C39, compression test was done on the cylindrical concrete specimens to determine the compressive strength of the concrete. The compression test was done every 7 days until the concrete reached the 28 days strength. The strength of the second placement concrete was 5900 psi after 28 days. The results of this test are shown in Appendix A. In addition, the ASTM C469 test was done on the cylindrical concrete specimens in order to determine the modulus of elasticity of the concrete at age 28 days. The concrete modulus of elasticity determined by this test was 4154 ksi and the results of this test are presented in Appendix A.

Similar to the small specimen corrosion process, the corrosion block outs were filled with saline solution, and a current intensity of 0.3 Amps was put through them. Since the full scale specimen was located outside, the weather was cold and each duct consisted of more strands, 0.3 A was not enough current intensity to corrode the tendons. Therefore, the current intensity was increased to 2 A and the saline solution with 15% concentration was used. After 216 hours all of the strands were broken, and the tendons were fully dissolved. The results of the corrosion test for the full scale specimen is discussed in more detail in the next Chapter (Chapter 4).

3.3 Computer Modeling

The objective of the computer modeling was to compare the collected data from the full-scale specimen with the data obtained from the analysis. A finite element model was designed similar to the full scale specimen: a 75 ft long slab with the width of 3 ft- 4 in. and 9 in. thickness. There were two tendons in the slab with 20 in. spacing, and in each duct, there were four 0.6 in. diameter strands. The model was designed to recreate the same behavior of tendons in the smooth ducts similar to the full scale specimen and the Varina-Enon Bridge. The end section of the slab was designed to have a thickness of 3 ft and the ducts curved to match the Varina-Enon Bridge plans. Figure 3-25 shows the computer model of the full scale specimen.

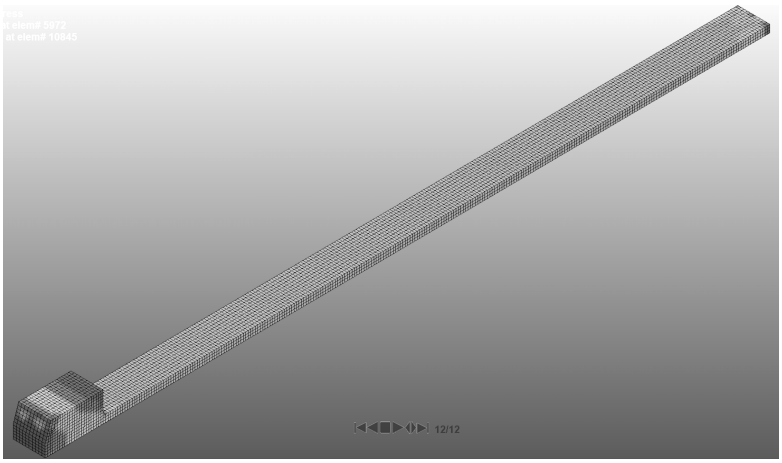

Figure 3-25 Computer Model of the Full Scale Specimen

For the most accurate results, the material properties such as concrete modulus of elasticity were modeled according to the full-scale specimen. Moreover, this finite element model provided more information in order to have a better understanding of the behavior of the full scale specimen. The result of the computer model is discussed in more detail in the next chapter.

4. RESULTS

This chapter focuses on the result obtained from the full scale specimen and the finite element model. The results from the corrosion test for the full specimen are discussed in this chapter. In addition, the results from BDI gauges and LVDT sensors located on the full scale specimen are discussed in detail. Also, the results from finite element model are presented to confirm the data obtained from the full scale specimen

4.1 Full Scale Specimen Results

This section presents the results that were obtained from the full scale specimen. For instance, pictures from the corrosion process for both well grouted and poorly grouted ducts are provided. The BDI gauges were important in two stages of the experiment: first in confirming the strain in the concrete with the calculation after prestressing, and secondly by showing any sudden changes in the concrete strain that would indicate a wire failure. In addition, LVDT were installed at the end section to recognize any movement at of the pour-backs.

4.1.1 Corrosion Test Results

As it was mentioned before in the previous chapter, the corrosion process for the full scale specimen was longer than the small specimen due to greater steel cross section and the environmental condition. Therefore, after conducting the corrosion process for 216 hours, all of the strands fractured, and the tendons were fully dissolved. In both poorly grouted and well grouted duct, the first break occurred within 48-72 hours. Figure 4-1 presents the progress in the strand corrosion process in the well grouted duct.

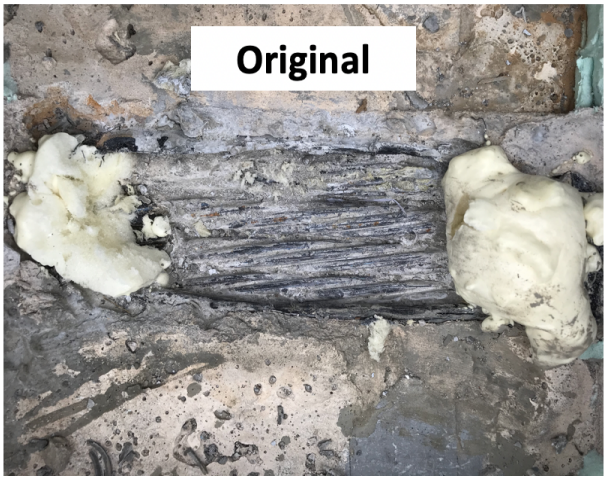
Original

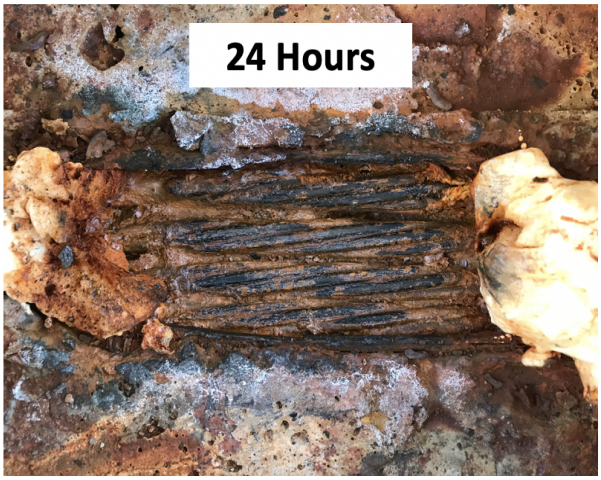
24 Hours


48 Hours


72 Hours

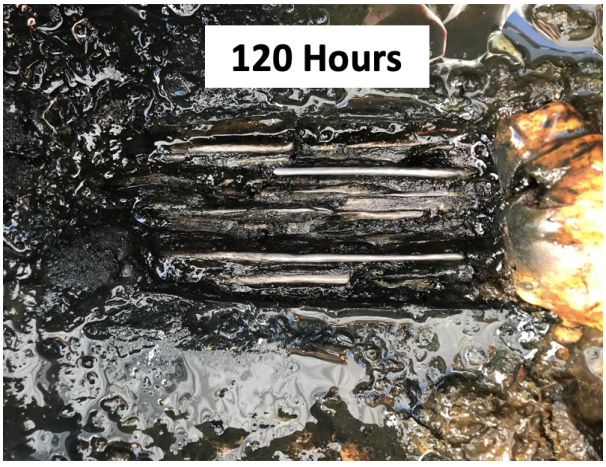
120 Hours

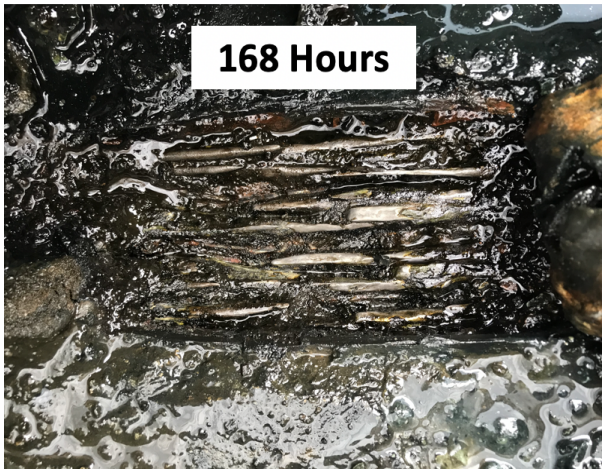
168 Hours

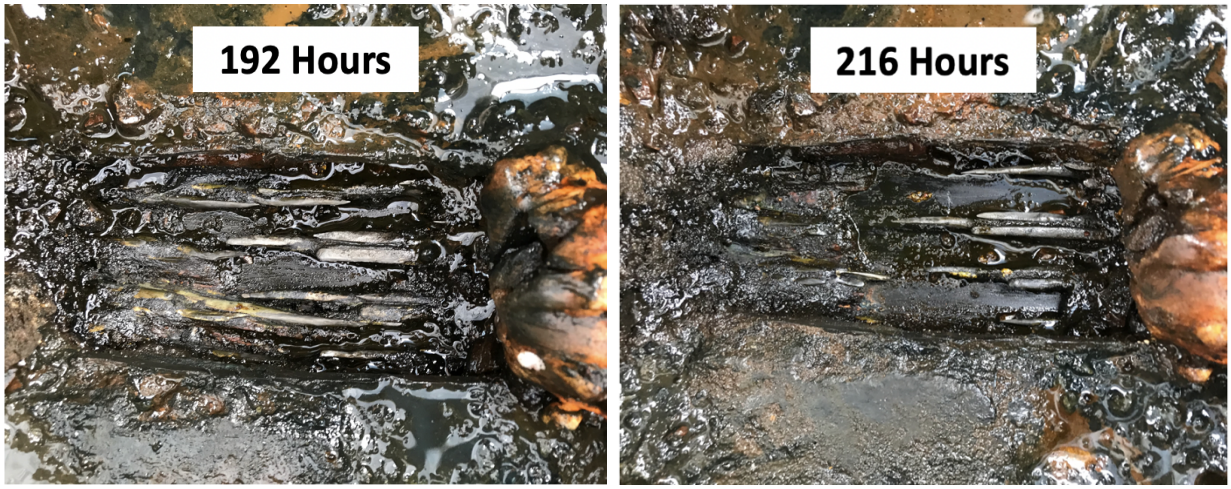

Figure 4-1 Progress in the Strand Corrosion in Well Grouted Duct

As mentioned before, the poorly grouted duct experienced the first break between 48-72 hours too, and it followed the same trend as the well grouted and the tendons were fully corroded and disconnected after 216 hours. Figure 4-2 shows the progress in the strand corrosion process in the poorly grouted duct.

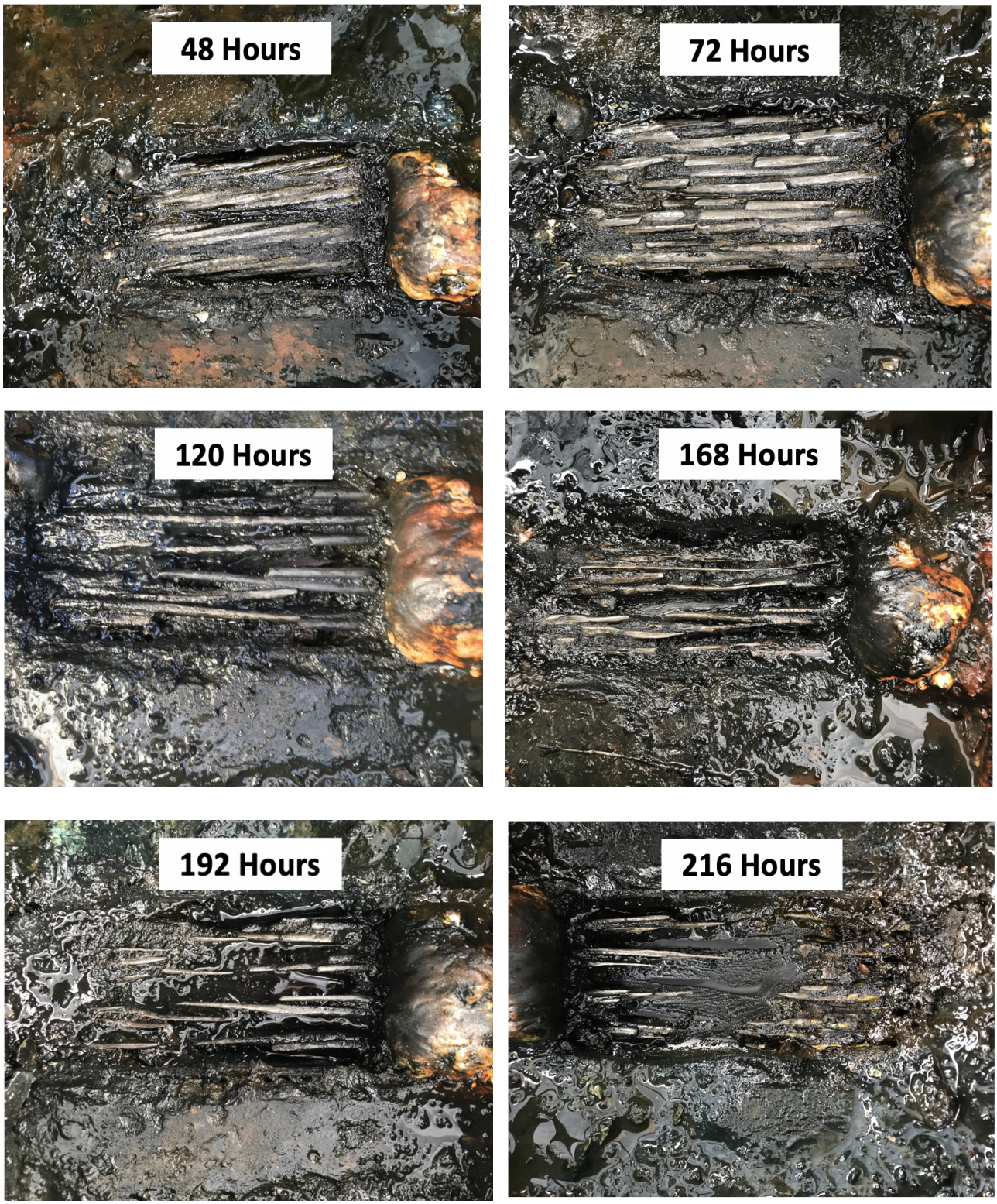

Figure 4-2 Progress in the Strand Corrosion in Poorly Grouted Duct

4.1.2 Instrumentation Result

As mentioned in the previous chapter, BDI strain gauges were installed on the full scale specimen before the prestressing process. The purpose was to be able to confirm the strain in the concrete with the calculated strain after all eight strands were stressed and to monitor strains as strands broke. Figure 4-3 shows a plan view of the slab with the locations of the BDI strain gauges.

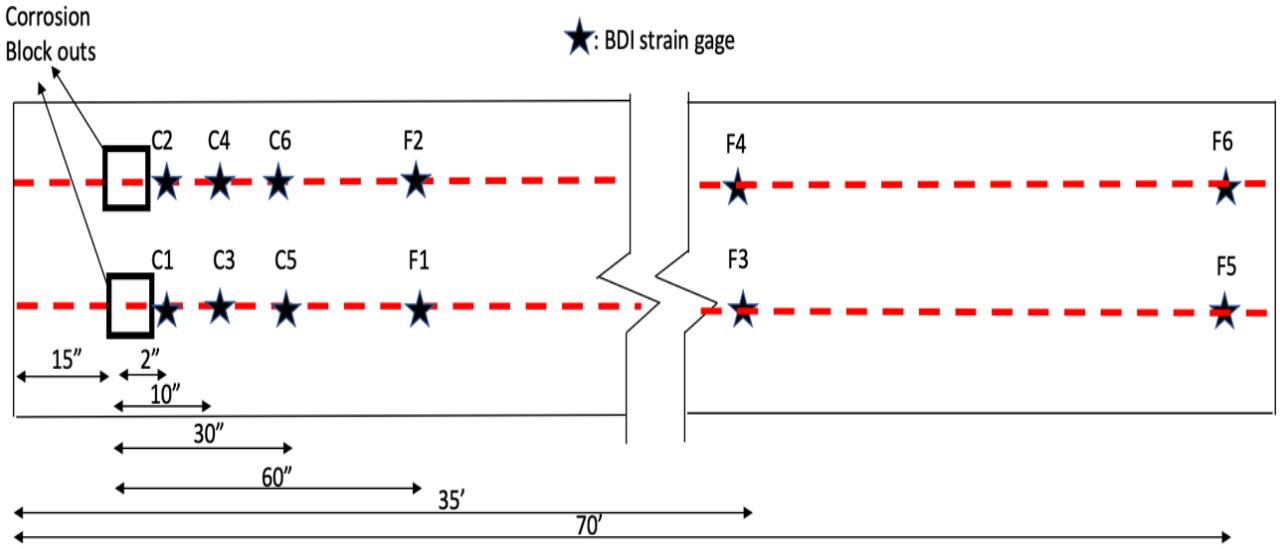

Figure 4-3 Locations of the BDI Strain Gauges on the Full Scale Slab

Figure 4-4 shows the strain in concrete measured by all the strain gauges three hours before and after the stressing of the tendons. To get a better understanding of the strain data, a graph for only one of the BDI gauges is provided below. Figure 4-5 shows the concrete strain captured by strain gauge 5 (Close 5).

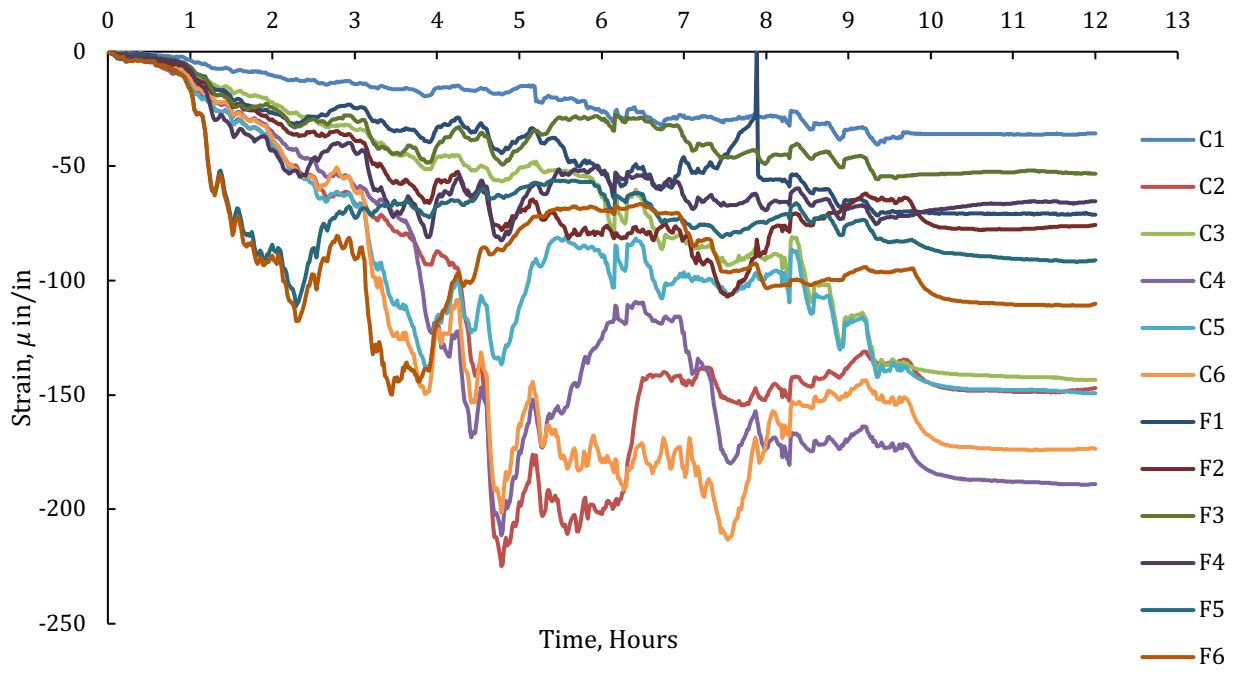

Figure 4-4 Strain in Concrete Before, during and after the stressing of the tendons

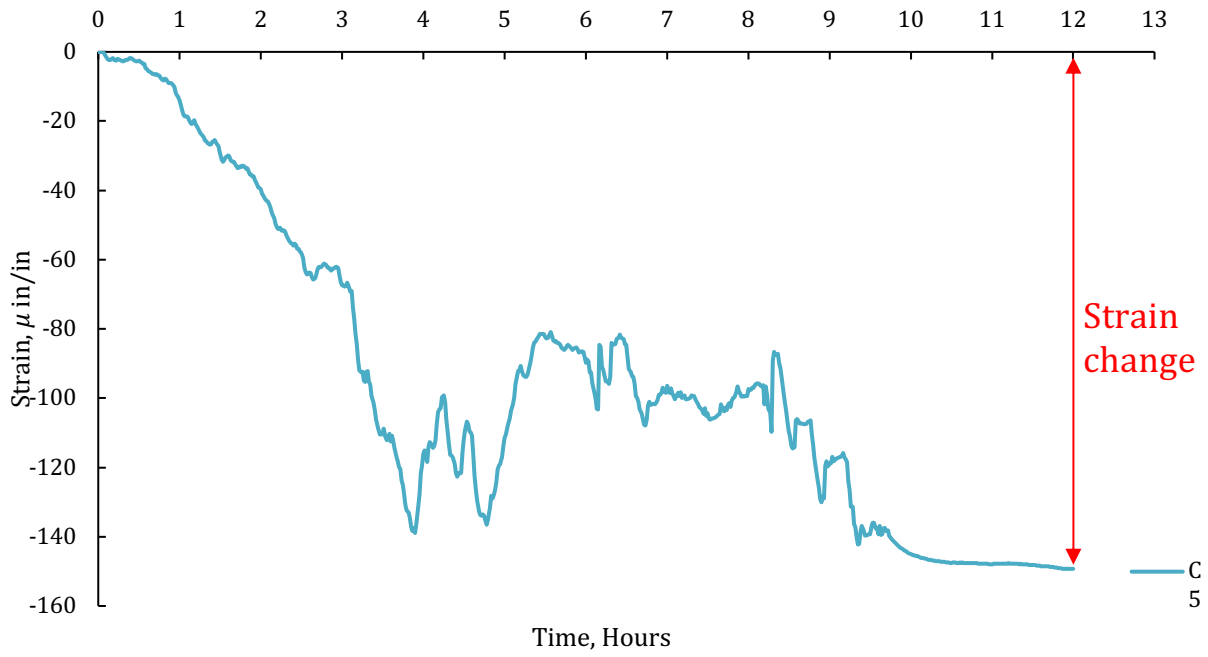

Figure 4-5 Strain in Concrete Captured by Strain Gauge C5

The curves shown in Figure 4-4 follow the same trend, with a clear change in the concrete strain during the prestressing operation. The significant fluctuations of the strain values during the stressing operation are attributed to various activities taking place on the specimen during the procedure. In Figure 4-5, the difference between the highest point and lowest point of the curve is shown with an arrow and it is the strain change in the concrete and it is about 161 $\mu\varepsilon$.

Calculations below shows the strain in the concrete after prestressing and table 4-1 presents detailed calculation of stress in each strand. As shown, the total prestressing force was calculated to be 258 kip and the calculated strain in concrete after prestressing was 163.8 $\mu\varepsilon$, which means the percentage error between the data from BDI gauges and calculated strain was only 1.22%. Therefore, that shows the BDI gauges are very accurate and the results from them matches the calculated concrete strain.

$$A = 354in^2 \qquad E = 4451\ ksi \qquad P = 258\ kip$$

$$\sigma = \frac{P}{A} = \frac{258\ kip}{354\ in^2} = 0.729\ ksi$$

$$\varepsilon = \frac{\sigma}{E} = \frac{0.729\ ksi}{4451\ ksi} \times 10^6 = 165.1\ \mu\varepsilon$$

$A : Cross - section\ area\ of\ concrete$

$E : Young's\ modulus\ of\ elasticity\ of\ concrete\ (calculated\ using\ test\ ASTM\ C469)$

P : *Total prestress force in all the tendons combined*

Table 4-1 Detailed Calculation of Stress in Each Strand

Calculating the strain in each tendon after stressing						
Tendon						
E	28500	ksi	$\delta = \frac{P*L}{E*A}$			
A	0.217	in^2				
L	75	ft				
Po	38	kip				
North				South		
Tendon 1				Tendon 1		
Seating loss	1.75	in		Seating loss	0.375	in
P loss due to seating	12.0	kip		P loss due to seating	2.6	kip
ΔP	26.0			ΔP	35.4	
Tendon 2				Tendon 2		
Seating loss	0.5	in		Seating loss	0.3125	in
P loss due to seating	3.4	kip		P loss due to seating	2.1	kip
ΔP	34.6			ΔP	35.9	
Tendon 3				Tendon 3		
Seating loss	0.5	in		Seating loss	1.5	in
P loss due to seating	3.4	kip		P loss due to seating	10.3	kip
ΔP	34.6			ΔP	27.7	
Tendon 4				Tendon 4		
Seating loss	0.5	in		Seating loss	0.5	in
P loss due to seating	3.4	kip		P loss due to seating	3.4	kip
ΔP	29.5			ΔP	34.6	
Concrete						
f'c	6000	ksi	$\sigma = E\varepsilon$			
E	4415.2	ksi				
A	354	in^2				
Sum of all the forces goint to concrete		258.10	kip			
σ	0.729					
ε	0.000165					
	165.1	$\mu\varepsilon$				

Results show strain in the concrete decreases as the location of strain gauges is further from the stressing end. For better comparison, for each two strain gauges close to each other, a separate graph was drawn. Figures 4-6 a - f show strain in the concrete at different along the slab. Strain in concrete starts from 168 $\mu\varepsilon$ at location of C1 and C2 and decreases to 161 $\mu\varepsilon$ once it

gets to the location of C5 and C6. The change in the concrete strain is not noticeable, since all these strain gauges were located very close to each other and within the development length of the strands. However, as the strain gauges were further form the stressing end, they experienced a significant decrease in the strain in the concrete. For instance, strain in the concrete at location of F5 and F6 decreases to 59.5 $\mu\varepsilon$,which represents a 64% decrease in the concrete strain compare to the locations close to the stressing end.

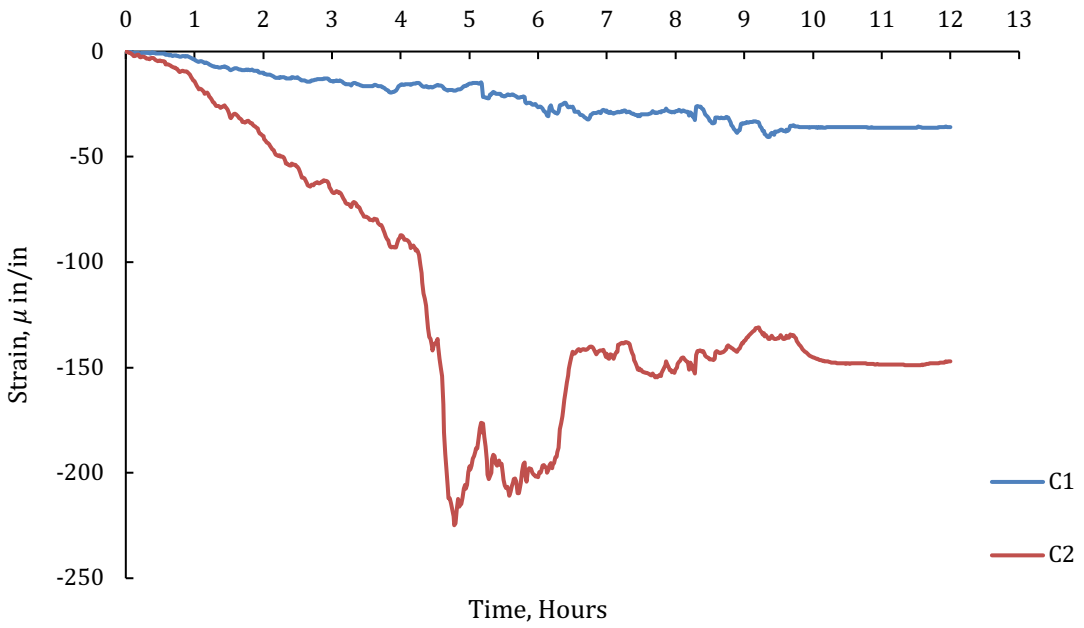

a)

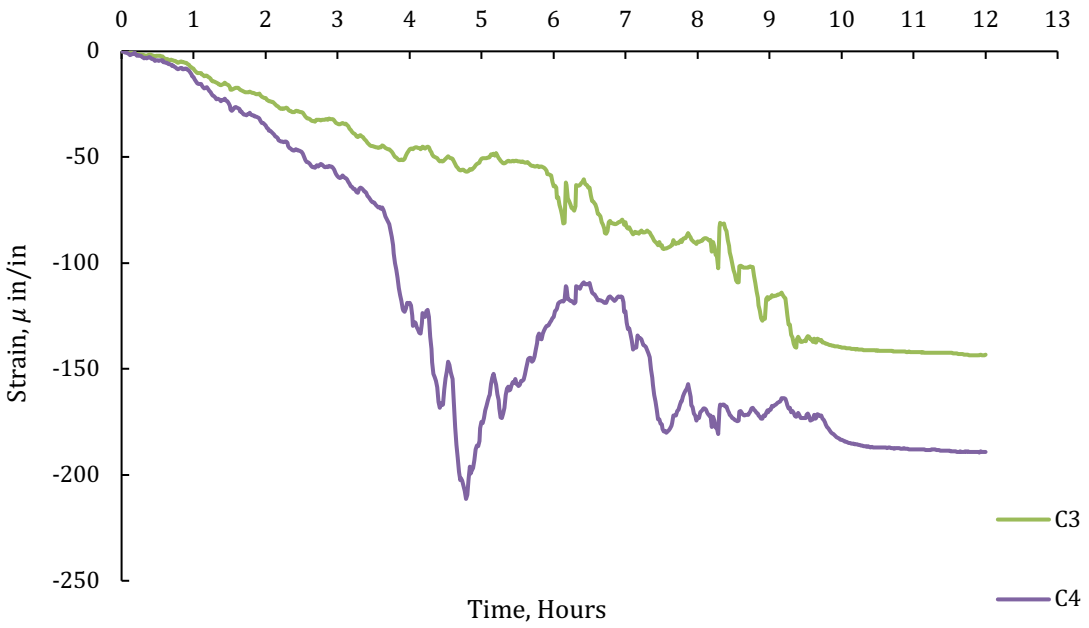
0
1
2
3
4
5
6
7
8
9
10
11
12
13
0
-50
-100
-150
-200
-250
Strain, μ in/in
Time, Hours
C3
C4

b)

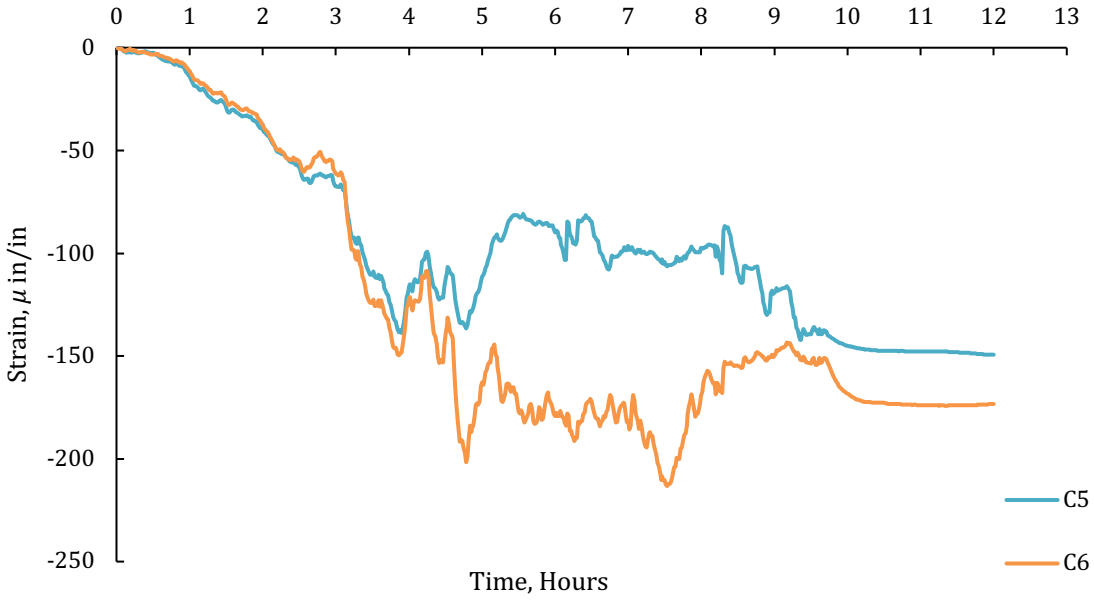
0
1
2
3
4
5
6
7
8
9
10
11
12
13
0
-50
-100
-150
-200
-250
Strain, μ in/in
Time, Hours
C5
C6

c)

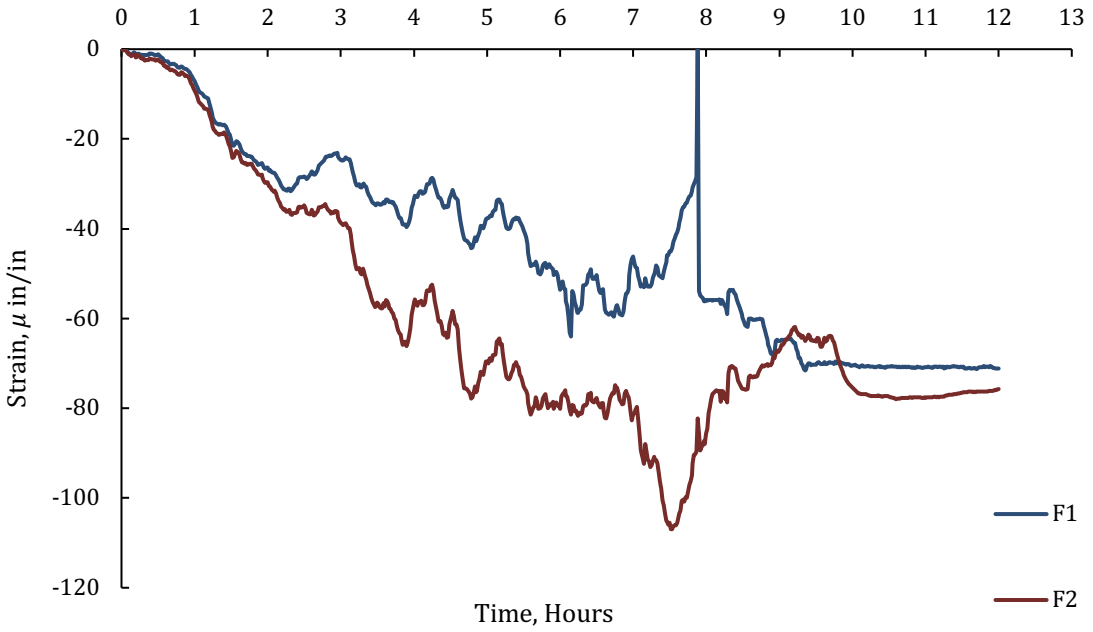
0 1 2 3 4 5 6 7 8 9 10 11 12 13
0
-20
-40
-60
-80
-100
-120
Strain, μ in/in
Time, Hours
F1
F2

d)

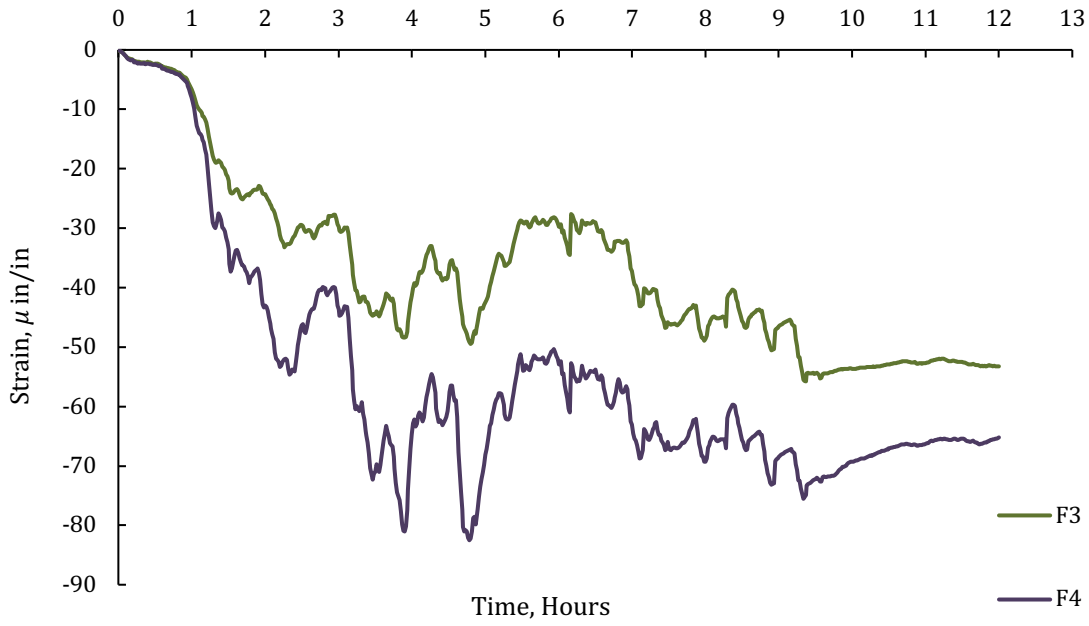
0 1 2 3 4 5 6 7 8 9 10 11 12 13
0
-10
-20
-30
-40
-50
-60
-70
-80
-90
Strain, μ in/in
Time, Hours
F3
F4

e)

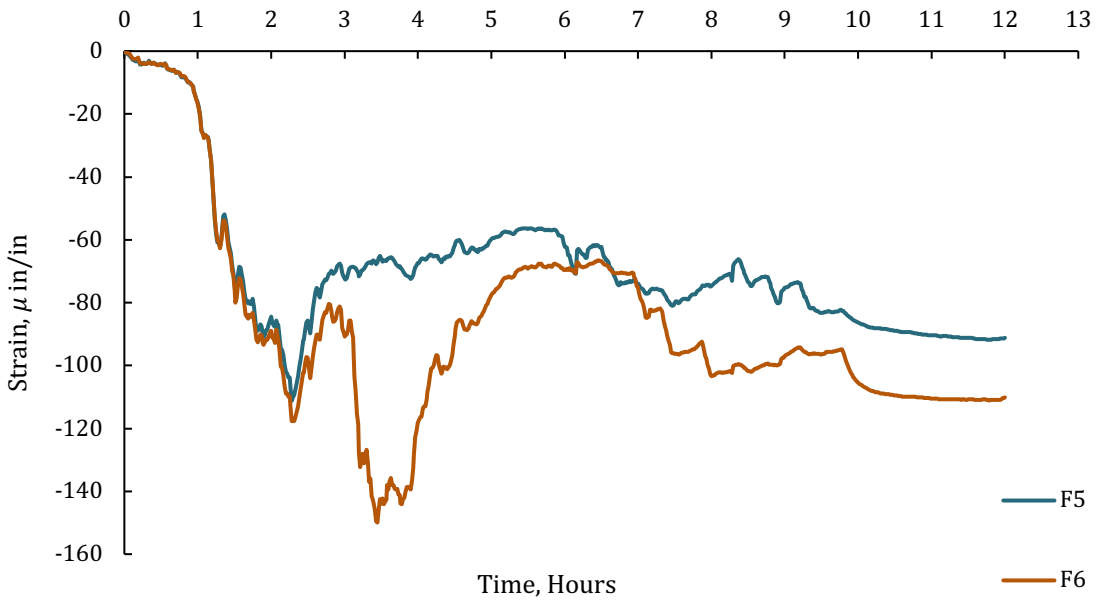

f)

Figure 4-6 Strain in the Concrete at Different Locations of Strain Gauges

During the corrosion process the strain evolution was closely monitored to capture any sudden change in the strain which would indicate a wire failure. Figure 4-7 presents the strain in the concrete measured by all the BDI gauges during the corrosion process. As mentioned before, the first wire break occurred between 48-72 hours after the corrosion process began and within this period six BDI gauges captured a sudden change in the strain.

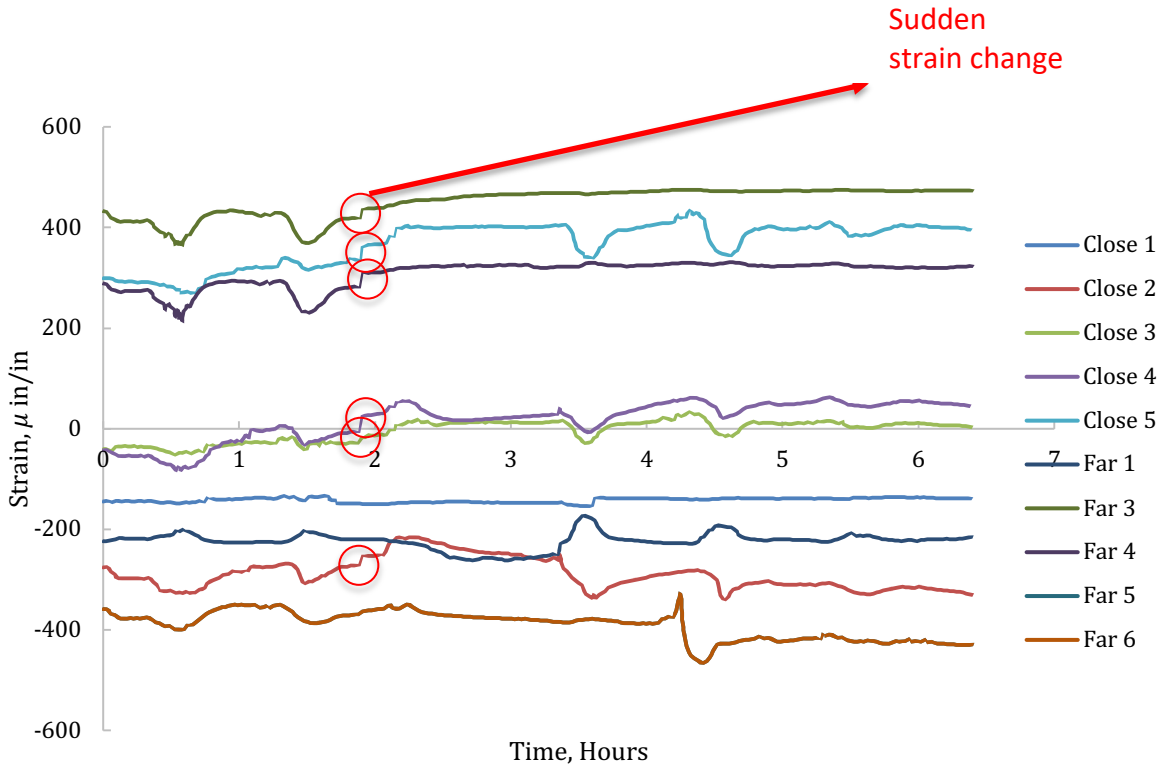

Figure 4-7 Strain in Concrete Captured by BDI Gauges During Corrosion Processes

The circled areas show the first wire failure in the tendons that was captured by six BDI gauges in different locations. C2, C4 and F4 gauges were located along the good grouted duct and C1, C5, and F3 were located along the poorly grouted duct. That means different gauges confirmed the first wire break in both ducts within 48-72 hours after the corrosion process. In order to get a better observation of this sudden change, data from F4 strain gauge was plotted separately in Figure 4-8.

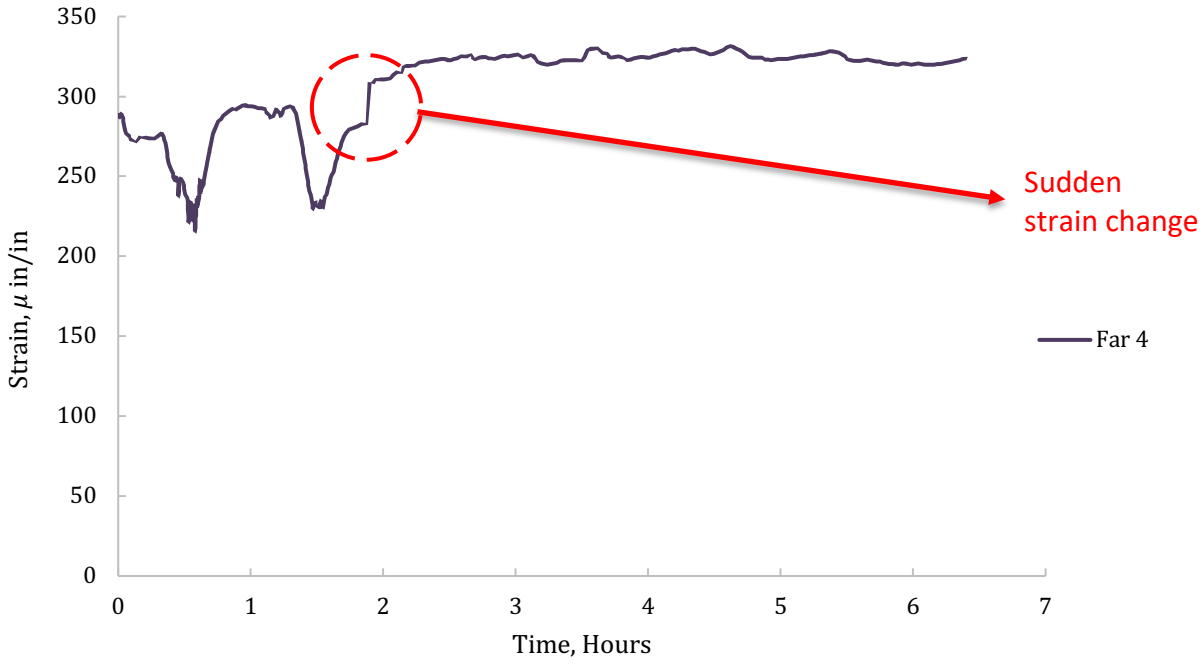

Figure 4-8 Strain in Concrete Captured by BDI Gauge F4 During Corrosion Processes

Figure 4-8 shows that BDI gauge F4 captured the changes in the concrete strain during the corrosion process and how it's gradually changing. However, the circled area is the only spot on the graph that strain change is sudden and might indicate the wire failure.

BDI gauges installed on the full scale specimen were very sensitive and the data obtained from them confirms the concrete strain after prestressing and only the first wire failure. Moreover, as research shows, more reliable sensors to capture the wire beak in tendons will be acoustic emission systems. VDOT has a long-term plan to monitor the Varina-Enon Bridge closely in the future. This includes, installing instrumentations such as BDI strain gauges on the bridge in the critical locations. This research shows how BDI gauges will be very helpful in reading the strain in the concrete and capturing the strain loss in the concrete, however in order to detect any wire failure, other types of instrumentations are required.

Also, pour-back material in the block out pockets on the inside of the Varina-Enon Bridge appear to have been dislodged, possibly due to strand fractures. LVDT sensors were installed in the full scale specimen on the pour-backs at anchorage block-outs to recognize any movement at any of the pour-backs. However, the data obtained from the LVDT sensors did not show any movement near the block out and there was no change in pour-back material in the block out pocket.

4.2 Computer Modeling Results

The finite element model was created similar to the full scale specimen in order to confirm the results from the full scale specimen. For the most accurate results, the material properties such as concrete modulus of elasticity were modeled according to the full scale specimen. Since the model was designed to match all the full scale specimen parameters, it was expected to get similar result as the full scale specimen. As shown in the previous calculations, the calculated stress and strain at the stressing end concrete are 0.729 ksi and 163 $\mu\varepsilon$, respectively. Figure 4-9 shows the finite element model with the stress distribution after applying the prestress loads and the stress is in units of ksi. The maximum compressive stress at the stressing end was 0.7408 ksi which means the percentage error for the stress in the concrete was 1.6%. In addition, as it was expected, stress and strain of the concrete decreases along the slab as we go further form the stressing end.

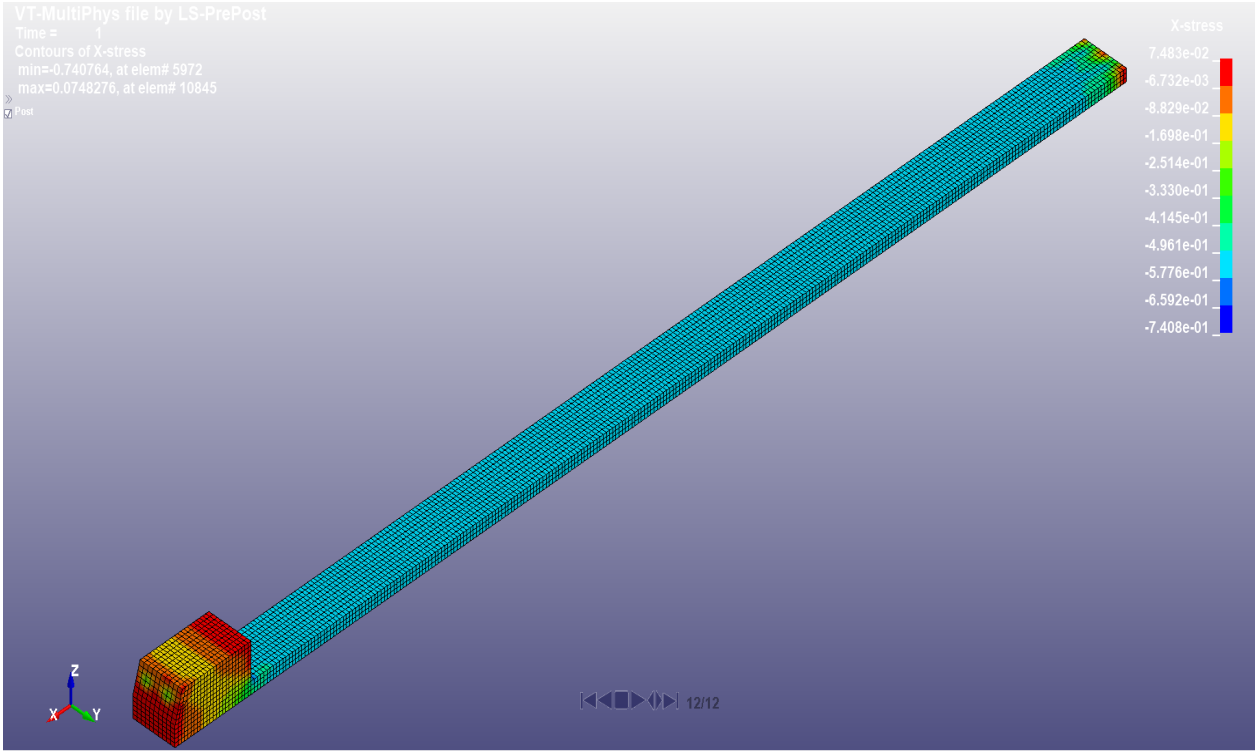

Figure 4-9 Stress Distribution in Finite Element Model

5. CONCLUSION

This chapter discusses the result from full scale specimen and how these this approach helped to achieve the objective of this project. In addition, these results will help to get a better understanding of the issues in the Varina-Enon Bridge and the possible solutions.

The following observations and conclusions are reached in the present study.

1. The finite element model was designed similar to the full scale specimen in order to confirm the results from the full scale specimen. The calculated strain at the stressing end in concrete matched the strain in the concrete obtained from the finite element model with only 1.6% percentage error. Also, the model confirmed that the strain in concrete decrease as we go further from the stressing end.
2. A Smooth flat duct was used in the full scale specimen however, the tendons did not move or slide in the ducts. That means the slipping of the strand in the grouted duct in the Varina-Enon Bridge should not occur, even though ducts are smooth.
3. Two different qualities of grouting were used for full scale specimen: one duct was good grouted and the other one poorly grouted. The poor grouting did not have any effect on the bond between the grout and the strands, and the strands did not slip in any of the ducts.
4. The strain gauges installed on the full-scale specimen were very sensitive, and the data obtained from them, confirmed the concrete strain after prestressing with calculations and the finite element model. In addition, they can identify the stain loss in the concrete.

However, they only captured the first wire failure and different types of instrumentations are needed in order to detect the wire failure.

5. LVDT sensors were installed in the full-scale specimen on the pour-backs at anchorage block-outs to recognize any movement at of the pour-backs when the strands fail. However, the data obtained from the LVDT sensors didn't show any movement near the block out. That means the dislodged pour-back material in the block out pockets wasn't due to the strand fracture.
6. The results from the BDI strain gauges showed that the strain in the concrete decreases as the location of strain gauges is further from the stressing end. That means if the strand failure is closer to the wind tip of the box girder in the Varina-Enon Bridge, the strand will fully be developed by the time it gets closer to the box girder, so the concrete box girder will not experience much strength lose.

6. RECOMMENDATION

The Varina-Enon Bridge is a critical link in the Richmond Transportation System, and it is important for VDOT to maintain this bridge at its best condition. The following includes the recommendations regarding this bridge:

1. As the BDI strain gauges were able to only detect the first wire failure, more reliable sensors are needed, and research shows acoustic emission systems are very effective to detect the wire failure even in the bridges in service.
2. Use the results of this project to help to develop an instrumentation system to monitor the critical locations in the bridge for future studies.
3. A model of the main cable stayed spans of the Varina-Enon Bridge is needed to study and investigate the causes of the transverse tendon breaks. In addition, the model which will include effects of traffic loading.
4. Since this research shows the poor grouting and the smooth duct were not the reasons of the tendon shooting out of the concrete in the bridge and they can provide enough bond at the service level loads, more extensive research is needed to investigate this issue.

7. REFFERENCES

Abdullah, A. B. M., et al. “Full-Scale Experimental Investigation of Wire Breakage Detection in Deviated Multi-Strand Tendon Systems.” *Journal of Civil Structural Health Monitoring*, vol. 6, no. 2, Apr. 2016, pp. 217–35. *Crossref*, doi:10.1007/s13349-016-0158-7.

Castel, A., et al. “Structural Response of Corroded, Unbonded Posttensioned Beams.” *Journal of Structural Engineering*, vol. 137, no. 7, July 2011, pp. 761–71. *Crossref*, doi:10.1061/(ASCE)ST.1943-541X.0000315.

Castel, Arnaud, et al. “Response of Corroded Prestressed Beams with Bonded Strands.” *Proceedings of the Institution of Civil Engineers - Structures and Buildings*, vol. 165, no. 5, May 2012, pp. 233–44. *Crossref*, doi:10.1680/stbu.10.00023.

“Response of Corroded Prestressed Beams with Bonded Strands.” *Proceedings of the Institution of Civil Engineers - Structures and Buildings*, vol. 165, no. 5, May 2012, pp. 233–44. *Crossref*, doi:10.1680/stbu.10.00023.

Cheong, Kah Kian, et al. “Evaluation of Grouting Condition of Post-Tensioned Concrete Using R-Wave Method.” *E3S Web of Conferences*, edited by Y.F. Huang et al., vol. 65, 2018, p. 02004. *Crossref*, doi:10.1051/e3sconf/20186502004.

Coronelli, Dario, et al. “Corroded Post-Tensioned Beams with Bonded Tendons and Wire Failure.” *Engineering Structures*, vol. 31, no. 8, Aug. 2009, pp. 1687–97. *Crossref*, doi:10.1016/j.engstruct.2009.02.043.

Cullington, D. .., et al. “Continuous Acoustic Monitoring of Grouted Post-Tensioned Concrete Bridges.” *NDT & E International*, vol. 34, no. 2, Mar. 2001, pp. 95–105. *Crossref*, doi:10.1016/S0963-8695(00)00034-7.

"Continuous Acoustic Monitoring of Grouted Post-Tensioned Concrete Bridges." *NDT & E International*, vol. 34, no. 2, Mar. 2001, pp. 95–105. *Crossref*, doi:10.1016/S0963-8695(00)00034-7.

Fernandes, Bertrand, et al. "A New Magnetic Sensor Concept for Nondestructive Evaluation of Deteriorated Prestressing Strand." *Research in Nondestructive Evaluation*, vol. 23, no. 1, Jan. 2012, pp. 46–68. *Crossref*, doi:10.1080/09349847.2011.626143.

FIGG. (2016). Retrieved from http://www.figgbridge.com/varina_enon_bridge.html

Fricker, Stephan, and Thomas Vogel. "Site Installation and Testing of a Continuous Acoustic Monitoring." *Construction and Building Materials*, vol. 21, no. 3, Mar. 2007, pp. 501–10. *Crossref*, doi:10.1016/j.conbuildmat.2006.04.008.

Kamalakannan, Suruthi, et al. "Factors Affecting the Performance Characteristics of Cementitious Grouts for Post-Tensioning Applications." *Construction and Building Materials*, vol. 180, Aug. 2018, pp. 681–91. *Crossref*, doi:10.1016/j.conbuildmat.2018.05.236.

Li, Fumin, and Yingshu Yuan. "Effects of Corrosion on Bond Behavior between Steel Strand and Concrete." *Construction and Building Materials*, vol. 38, Jan. 2013, pp. 413–22. *Crossref*, doi:10.1016/j.conbuildmat.2012.08.008.

Minh, Ha, et al. "Influence of Grouting Condition on Crack and Load-Carrying Capacity of Post-Tensioned Concrete Beam Due to Chloride-Induced Corrosion." *Construction and Building Materials*, vol. 21, no. 7, July 2007, pp. 1568–75. *Crossref*, doi:10.1016/j.conbuildmat.2005.10.004.

Wang, Lei, et al. “Effect of Insufficient Grouting and Strand Corrosion on Flexural Behavior of PC Beams.” *Construction and Building Materials*, vol. 53, Feb. 2014, pp. 213–24. *Crossref*, doi:10.1016/j.conbuildmat.2013.11.069.

Yong-Sik, Yoon, et al. “Effect of Grout Conditions and Tendon Location on Corrosion Pattern in PS Tendon in Grout.” *Construction and Building Materials*, vol. 186, Oct. 2018, pp. 1005–15. *Crossref*, doi:10.1016/j.conbuildmat.2018.08.023.

Yuyama, S., et al. “Detection and Evaluation of Failures in High-Strength Tendon of Prestressed Concrete Bridges by Acoustic Emission.” *Construction and Building Materials*, vol. 21, no. 3, Mar. 2007, pp. 491–500. *Crossref*, doi:10.1016/j.conbuildmat.2006.04.010.

Zhang, Xuhui, et al. “Corrosion-Induced Flexural Behavior Degradation of Locally Ungrouted Post-Tensioned Concrete Beams.” *Construction and Building Materials*, vol. 134, Mar. 2017, pp. 7–17. *Crossref*, doi:10.1016/j.conbuildmat.2016.12.140.

APPENDIX A

A1. Theoretical and Net Elongation for Small Specimen

Theoretical Elongation for West Strand:

Assumed values:

Wobble Coefficient: $k := 0.001 \cdot \frac{1}{ft}$

Friction coefficient: $\mu := 0.25$

Area of 0.5" diameter strand: $A := 0.153\ in^2$

Tendon path assumed to be straight: $\alpha := 0$

$L := 12.5\ ft$ Length of the strand

$E := 28500\ ksi$ Modulus of elasticity

$P_{jack} := 270\ ksi \cdot 0.75 \cdot A = 30.98\ kip$

$x_1 := 12.5\ in$ $\alpha := 0$ $P_1 := P_{jack} \cdot e^{-(\mu \cdot \alpha + k \cdot x_1)} = 30.95\ kip$

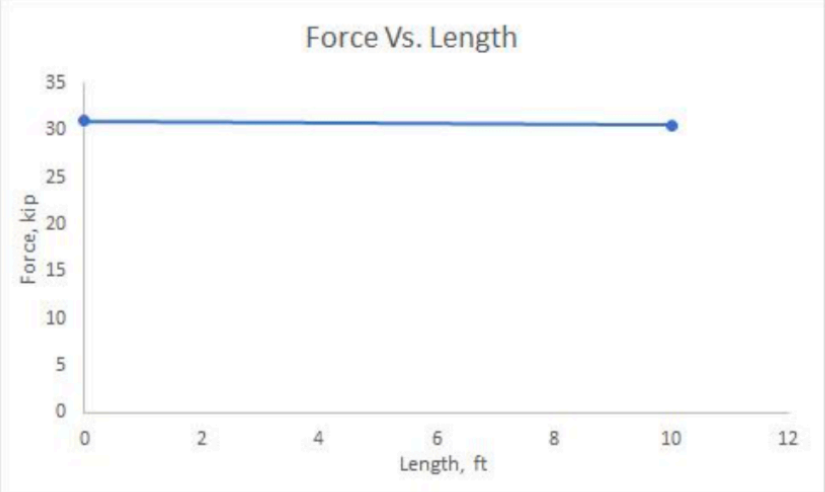

Area underneath the force vs. length diagram: $A_{total} := 384.875\ kip \cdot ft$

$\delta := \frac{A_{total}}{A \cdot E} = 1.06\ in$

APPENDIX A

Net Elongation for West Strand:

Load (kip)	Displacement (in)
	West
6	1.00
12	1.25
18	1.56
24	1.88
31	2.19
Dead end seat (in)	0.13
Ram wedge seat (in)	0.13

Factored elongation: $\delta_{Factored} := \left(\frac{2.19\ in - 1\ in}{31\ kip - 6\ kip}\right) \cdot 31\ kip = 1.48\ in$

Elongation in ram: $l_{ram} := 3\ ft$ $\delta_{ram} := \frac{P_{jack} \cdot l_{ram}}{A \cdot E} = 0.26\ in$

Dead End seat: $\delta_{dead} := 0.13\ in$

Ram wedge seat: $\delta_{ram.wedge} := 0.13\ in$

$\delta_{net} := \delta_{Factored} - \delta_{ram} - \delta_{dead} - \delta_{ram.wedge} = 0.96\ in$

APPENDIX A

A2. Theoretical and Net Elongation for Full Scale Specimen

Theoretical Elongation for North Tendon 3:

Assumed values:

Wobble Coefficient: $k := 0.001 \cdot \frac{1}{ft}$

Friction coefficient: $\mu := 0.25$

Area of 0.6" diameter strand: $A := 0.217\ in^2$

$\alpha_1 := 0.1125$ $\alpha_2 := 0.389$

$P_{jack} := 270\ ksi \cdot 0.65 \cdot A = 38.08\ kip$

Tendon Profile:

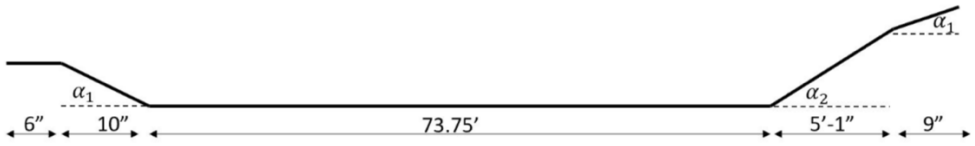

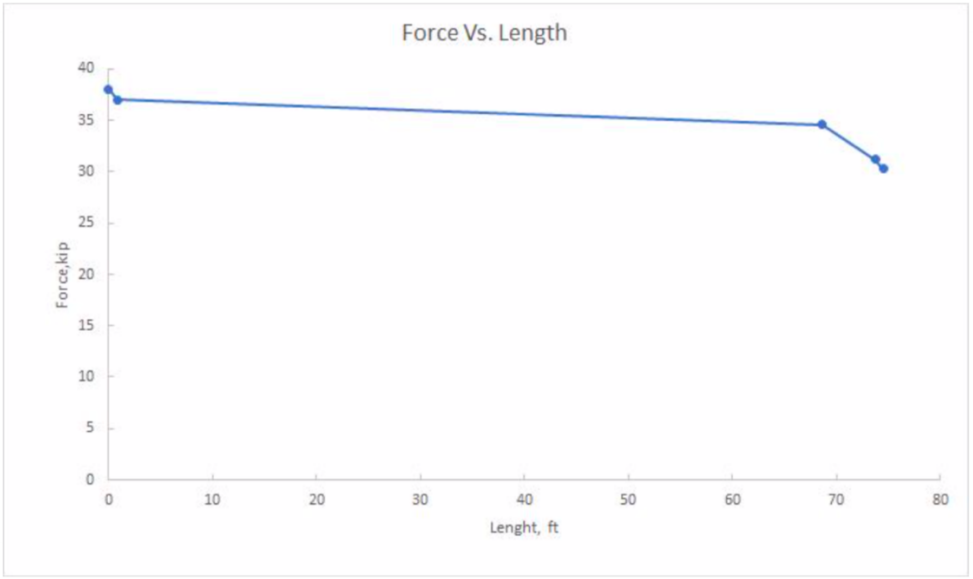

APPENDIX A

$x_1 := 10\ \text{in}$ $\quad \alpha := \alpha_1$ $\quad P_1 := P_{jack} \cdot e^{-(\mu \cdot \alpha + k \cdot x_1)} = 37\ \text{kip}$

$x_2 := 67.83\ \text{ft}$ $\quad \alpha := 0$ $\quad P_2 := P_1 \cdot e^{-(\mu \cdot \alpha + k \cdot x_2)} = 34.57\ \text{kip}$

$x_3 := 5\ \text{ft} + 1\ \text{in}$ $\quad \alpha := \alpha_2$ $\quad P_3 := P_2 \cdot e^{-(\mu \cdot \alpha + k \cdot x_3)} = 31.21\ \text{kip}$

$x_4 := 9\ \text{in}$ $\quad \alpha := \alpha_1$ $\quad P_4 := P_3 \cdot e^{-(\mu \cdot \alpha + k \cdot x_4)} = 30.32\ \text{kip}$

Area underneath the force vs. length diagram: $A_{total} := 2813.9\ \text{kip} \cdot \text{ft}$

$$\delta := \frac{A_{total}}{A \cdot E} = 5.46\ \text{in}$$

Net Elongation for North Tendon 3:

Load(kip)	North 3
4	5.00
14	6.63
22	7.94
30	9.19
38	10.50
Dead end seat (in)	0.13
Ram wedge seat (in)	0.5

$P := 38\ \text{kip}$

Factored elongation: $\delta_{Factored} := \left(\frac{10.5\ \text{in} - 5\ \text{in}}{38\ \text{kip} - 4\ \text{kip}}\right) \cdot 38\ \text{kip} = 6.15\ \text{in}$

Elongation in ram: $l_{ram} := 45\ \text{in}$ $\quad \delta_{ram} := \frac{P \cdot l_{ram}}{A \cdot E} = 0.28\ \text{in}$

Dead End seat: $\delta_{dead} := 0.13\ \text{in}$

Ram wedge seat: $\delta_{ram.wedge} := 0.5\ \text{in}$

$\delta_{net} := \delta_{Factored} - \delta_{ram} - \delta_{dead} - \delta_{ram.wedge} = 5.24\ \text{in}$

APPENDIX A

A3. Strength of the Concrete

First placement			
	Concrete strength		
Day	Cylinder 1	Cylinder 2	Average
0	0	0	0
11	6100	6000	6050
14	6320	6060	6190
21	6265	6880	6573
28	7060	6740	6900

Table A-1 First Placement Concrete Strength

Second placement			
	Concrete strength		
Day	Cylinder 1	Cylinder 2	Average
0	0	0	0
7	4415	4450	4433
14	5660	5220	5440
21	5750	5520	5635
28	5880	5920	5900

Table A-2 Second Placement Concrete Strength

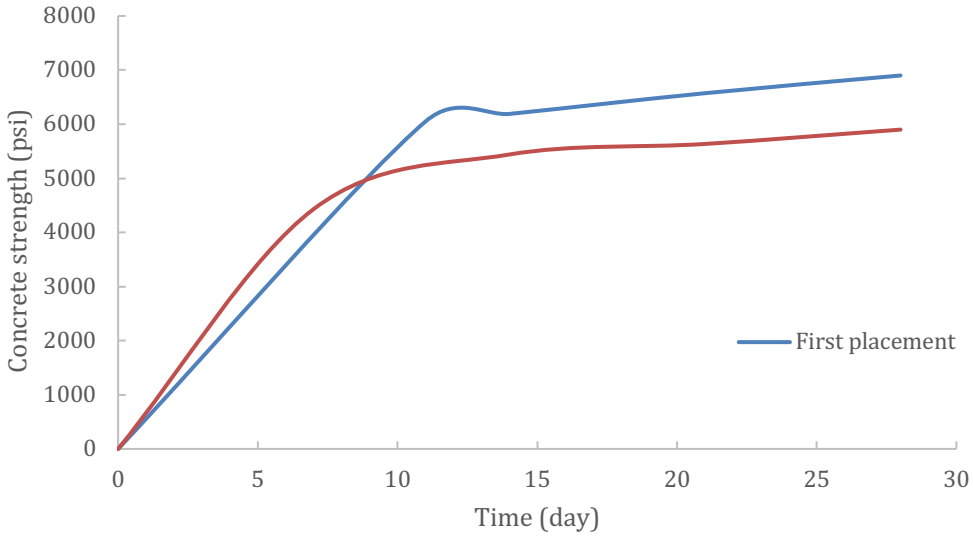

Figure A-1 Concrete Strength

APPENDIX A

A4. Modulus of Elasticity of the Concrete

Area of concrete cylinder: $A := 12.57\ in^2$

Length of concrete cylinder: $L := 5.5\ in$

Based on ASTM 469:

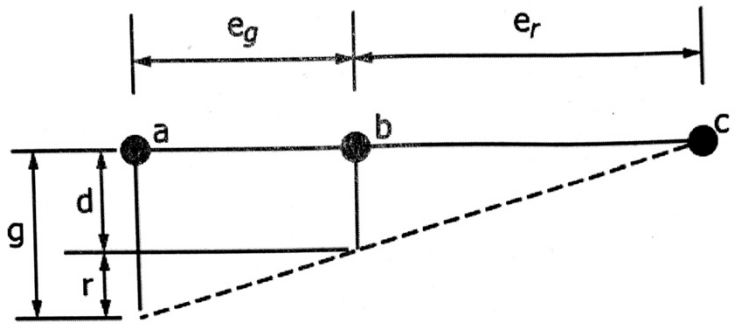

d = displacement due to specimen deformation
r = displacement due to rotation of the yoke about the pivot rod
a = location of gauge
b = support point of the rotating yoke
c = location of pivot rod
g = gauge reading

$eg := 2.75\ in$

$er := 2.75\ in$

$$Stress = \frac{Load}{A}$$

displacement $$\delta = \frac{g \cdot er}{(er + eg)}$$

$$Strain = \frac{\delta}{L}$$

APPENDIX A

Table A-3 First Cylinder data result Based on ASTM C469

First Cylinder				
Load (kip)	ΔL		Stress (ksi)	Strain (in/in)
0	0		0	0
4	0.00065		0.32	5.909E-05
8	0.0017		0.64	1.545E-04
13	0.0027		1.03	2.455E-04
16	0.00345		1.27	3.136E-04
20	0.0044		1.59	0.0004
24	0.0052		1.91	0.00047
E	3941	ksi		

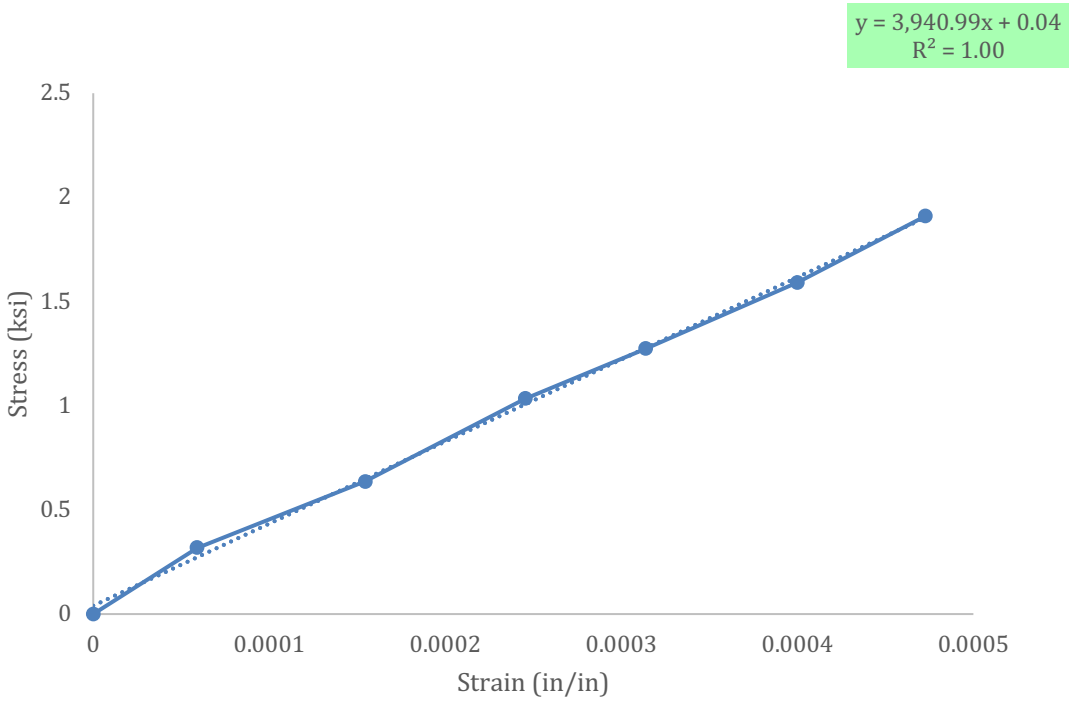

Figure A-2 Stress- Strain Curve for First Cylinder

APPENDIX A

Table A-4 Second Cylinder data result Based on ASTM C469

Second Cylinder				
Load (kip)	ΔL		Stress (ksi)	Strain (in/in)
0	0		0	0
5	0.001		0.40	9.091E-05
8	0.0017		0.64	1.545E-04
13	0.00275		1.03	0.00025
17	0.0037		1.35	0.00034
21	0.00435		1.67	0.00040
25	0.00525		1.99	0.00048
E	4149	ksi		

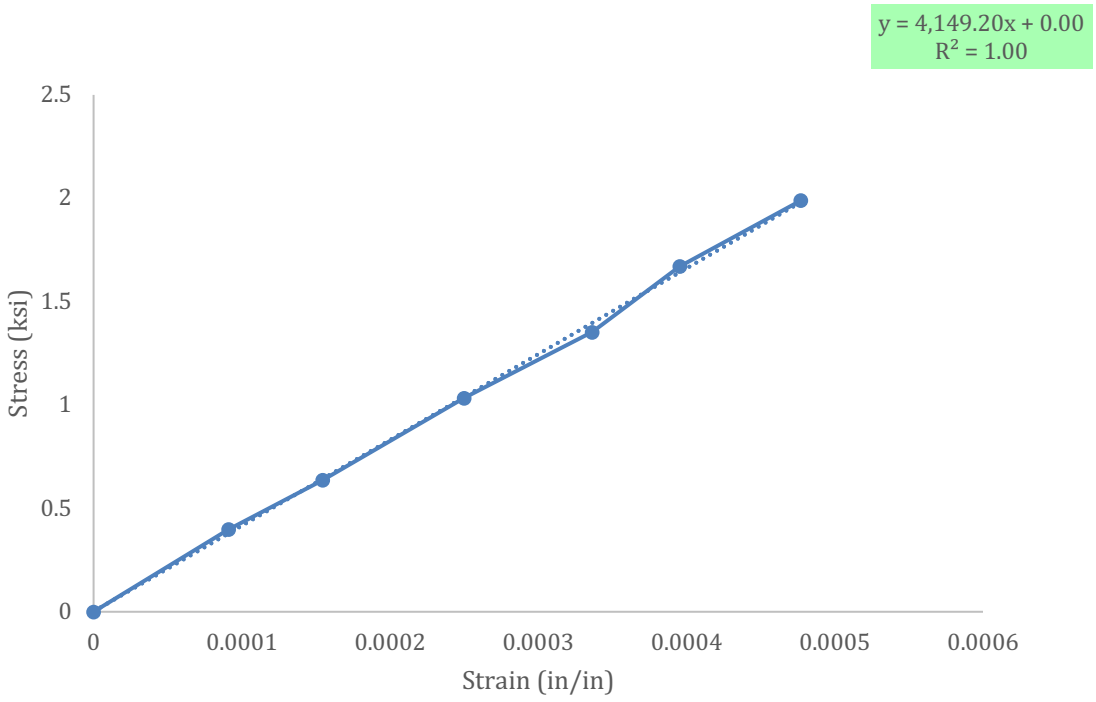

Figure A-3 Stress- Strain Curve for Second Cylinder

APPENDIX A

Table A-5 Third Cylinder data result Based on ASTM C469

Third Cylinder				
Load (kip)	ΔL		Stress (ksi)	Strain (in/in)
0	0		0	0
4	0.00075		0.32	6.818E-05
8.5	0.0019		0.68	1.727E-04
12	0.00255		0.95	2.318E-04
16.5	0.0036		1.31	3.273E-04
23	0.0047		1.83	0.0004273
E	4177	ksi		

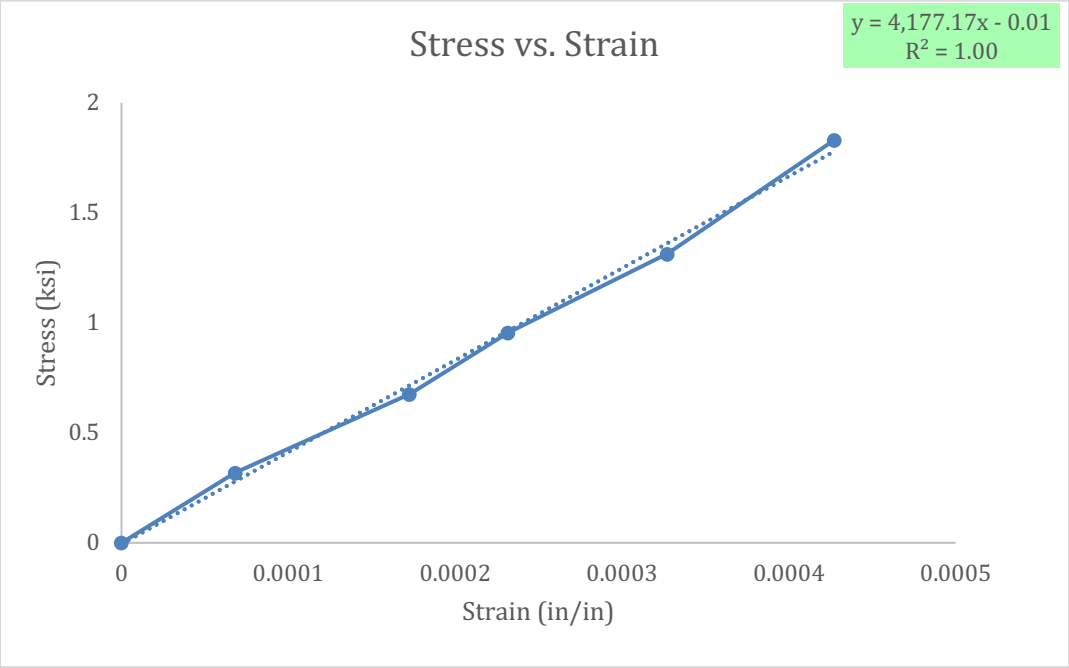

Figure A-4 Stress- Strain Curve for Third Cylinder

APPENDIX A

Table A-6 Fourth Cylinder data result Based on ASTM C469

Fourth Cylinder				
Load (kip)	ΔL		Stress (ksi)	Strain (in/in)
0	0		0	0
5.2	0.00125		0.41	1.136E-04
8.5	0.0019		0.68	1.727E-04
12	0.0025		0.95	0.0002273
16	0.00325		1.27	0.00030
22.5	0.0046		1.79	0.00042
26	0.00535		2.07	0.00049
E	4348	ksi		

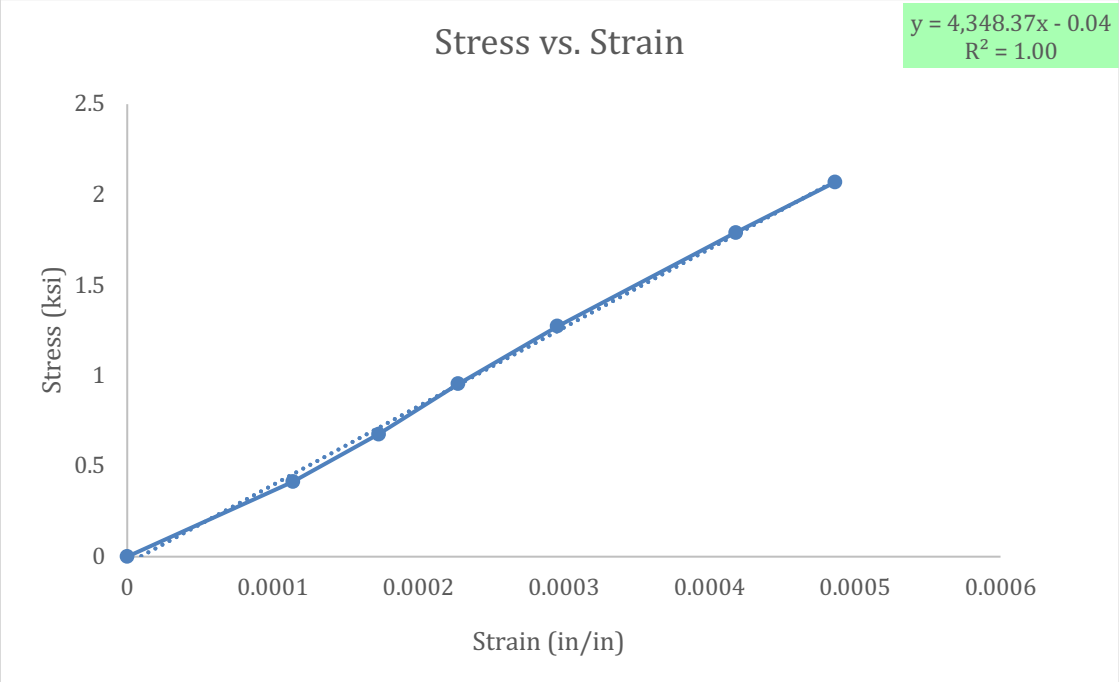

Figure A-5 Stress- Strain Curve for Fourth Cylinder